Research on Waveform Data of Radar Satellite Altimeters

王, 喜風

https://doi.org/10.15017/1807095

Research on Waveform Data of Radar Satellite Altimeters

by

Xifeng Wang

Interdisciplinary Graduate School of Engineering Sciences

Kyushu University

This thesis is presented for the

degree of Doctor of Philosophy

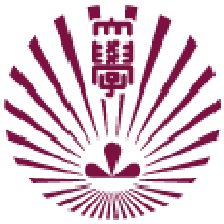

九州大学

KYUSHU UNIVERSITY

February 2017

ACKNOWLEDGEMENTS

I am deeply grateful to my supervisor Dr. Kaoru Ichikawa for the patient guidance, advice and help provided throughout my study time. I wish to thank Dr. Yoshinobu Wakata that have certainly contributed to this PhD work. I also wish to thank all of the friends, staffs and students in the Laboratory of Marine Environmental Physics for their help and encouragement. I also express my gratitude to all the researchers and students that I have met across this PhD time, and with whom I have had useful discussions. Special thanks to my family, whose patient love enabled me to complete this work.

ABSTRACT

Radar altimeters transmit modulated chirp pulses towards the sea at nadir, and then record the returned echoes which were reflected from the sea surface in an altimeter footprint. Time series of the power of received echoes by altimeters is usually known as "waveform". Geophysical parameters are retrieved by a process called "waveform retracking", which consists of fitting a theoretical model response to the measured waveforms. Over the open ocean, so-called Brown mathematical model is always treated as the standard model. The fundamental parameters derived from waveform retracking are the satellite height above the sea surface (range), the significant wave height (SWH) and the backscatter coefficient (σ_0) related to sea surface wind. In addition, subsequent studies have also indicated the possibility of retrieving a wave period parameter from SWH and σ_0 measurements of altimeters, and numerous empirical models have been proposed in the last two decades. Moreover, in contrast to open ocean, the radar altimeter data gathered over the coastal zones (particularly, within 10 km from the coastline) are always flagged as "bad" due to the issues of land contamination in the footprint and intrinsic difficulties in the geophysical corrections. In this thesis, two issues on waveform retracking are studied and described in separated parts I and Ⅱ; namely, wave period retrieval and waveform retracking over coastal zone, respectively.

Part Ⅰ: Recent researches have investigated the possibility of deriving an altimeter wave period parameter from the SWH and σ_0 measurements. Several retrieval models have been proposed, but the results of these studies show that wave periods estimated from satellite altimetry data behave differently from those calculated from buoy data, especially in low-wind conditions. In this thesis, the geometric mean wave period T_a is calculated from buoy data, rather than the commonly used zero-crossing wave period T_z. The geometric mean wave period uses the fourth moment of the wave frequency spectrum and is related to the mean-square slope of the sea surface measured using altimeters. The values of T_a obtained from buoys and altimeters agree well (root mean square difference: 0.2 s) only when the contribution of high-frequency sea waves is estimated by a wavenumber spectral model to complement the buoy data, because a buoy cannot obtain data from waves having wavelengths that are shorter than the characteristic dimension of the buoy.

Part Ⅱ: Altimeter waveforms are corrupted at coastal zones due to due to the heterogeneous reflective surfaces over altimeter footprint. The waveform corruption mainly consists of two types:

1) waveform corruption due to the effect of land contamination. Around the coastal area, the returned echoes reflected from the targets located above the mean sea surface such as land superimpose on the ocean returns. Generally, the power of land reflection is much weaker than that reflected from the sea surface. Even for the case of highly reflective point targets, like artificial construction, ship and iceberg etc., the echoes returned from these targets present as "speckle" noises and only appeared at the waveform thermal noise area. On the other hand, a power deficit can be seen in waveform trailing edge due to the weak reflection from land in altimeter footprint. The power deficit exceeded the normally decaying which controlled by the antenna beam pattern in the theoretical Brown model.

2) waveform corruption due to the inhomogeneous of the sea surface reflectivity. This is known to happen in particular for semi-closed seas, where the sea surface usually smoother than surrounding waters. The calm semi-closed seas can be seen as bright targets in the radar signal. Reflections from the calm water seriously corrupted waveforms and present as redundant peaks in the waveform trailing edge. Previous research has been pointed out that two of the predominant coastal waveform classes are quasi-specular and multi-peak waveforms. Both of them are connected with the presence of bright targets like calm water.

Since coastal waveforms are generally complicated, it is difficult to distinguish whether an echo is corrupted in a single waveform. In previous studies, sub-waveform retrackers which use only the waveform leading edge are recommended for coastal waveform ratracking. Different from the sub-waveform retrackers, the along-track waveforms (echogram) are used in this thesis considering its spatial distribution. In fact, the strong reflections from calm water obviously present as a parabola in the echogram. Utilizing the parabolic signature, these noises which are difficult to distinguish in individual waveform are explicitly selected and removed in this study. In addition, the power deficit due to weak land reflection is also compensated. The method has been performed to Jason-2 20Hz data around Tsushima in Japan. Results show that the correlation coefficient of sea surface height anomaly (SSHA) derived from altimeter and tide gauge measurements remains larger than 0.9 even at about 3km depart from coast. The root mean squared difference is about 20cm.

Keywords: radar altimeter; buoy; wave period retrieval; high-frequency sea wave; mean squares lope ; waveform retracking; land contamination; tide gauge.

CONTAINTS

1. Introduction…….....1

1.1 Altimeter Waveform Theory…..…..……..…….....2

1.1.1 Altimeter Waveform……..….....2

1.1.2 Waveform Retracking and Brown Model....……..….....4

1.2 Overview of Altimeter Wave Period Retrieval Models..…….7

1.3 Altimeter Waveform in the Coastal Zone…...…...…….8

1.3.1 Land Contamination Effect on Coastal Altimeter Waveform…….....8

1.3.2 Coastal Waveform Retracking Models....…….....13

1.4 Objectives and Organization of this Thesis……..……..…..…14

2. Part Ⅰ: Wave Period Retrieval by σ_0 and SWH.....15

2.1 Introduction.....15

2.2 Dataset……..….....15

2.3 Rationale of the Retrieval of Altimeter Wave Period.....16

2.4 Comparison of Geometric Mean Wave Periods Determined from Buoy and Altimeter Data….....19

2.5 Compensation of the Mean Square Slope Obtained Using the Buoy Data…….…….....23

2.6 Discussion.....28

2.7 Conclusions..……...……..…..…31

3. Par Ⅱ: Waveform Retracking over Tsushima in Japan……...32

3.1 Introduction…….....32

3.2 Dataset.....32

3.3 Waveform Modification Strategy…….....34

3.3.1 Detection and Mask of the Redundant peaks caused by calm waters….. 34

3.3.2 Compensation of the Power Deficit of Waveform Trailing Edge……..39

3.4 Results and Discussion……...42
3.5 Conclusions..……...……...……..44

4. Conclusions…….....46

References.....47

List of Figures

Figure 1-1. The pulse spherically expands to the sea surface at nadir (top); altimeter footprint varies with time (middle); the shape of waveform presents as a fast-rising leading edge and a gradually decaying trailing edge which depending on the antenna beam width. (http:// www. aviso. altimetry.fr)

Figure 1-2. Characteristics of typical Brown waveform over the open ocean.

Figure 1-3. Relationship between the height and distance to satellite nadir of a point target which returns could be received by Jason-2 altimeter.

Figure 1-4. Top: Raw echogram of Jason-2 over Tsushima (pass 36) on 2009.09.22 (cycle 45). Bottom: Re-scaled and re-aligned echogram corresponding to the top subplot. Black line represent the coastline.

Figure 1-5. Blue line is the ground track of Jason-2 altimeter over Tsushima (pass 36) on 2009.09.22 (cycle 45). Circles represent the pulse-limited altimeter footprint at the red point. The land area (red line) in the footprint lead to the power deficit of waveform trailing edge. The sea surrounded by land always present as "calm water" and seriously corrupt the shape of waveform.

Figure 1-6. Jason altimeter echo waveform in presence of circular slicks of 2 and 10 km radius and 10 and 5 dB relative brightness. (a) Schematic diagram showing the slicks (gray circles) and the altimeter footprint (circles, 1 per second). Modeled waveforms for the (b) 2 km radius and 10 dB brightness slick, (c) 10 km radius and 5 dB brightness slick, and (d) 20 km radius and 5 dB brightness slick. The waveform color scale is in arbitrary units (1 correspond to the maximum value of the Brown model). (Tournadre et al., 2006)

Figure 1-7. Schematic representation of the waveforms classes within the PISTACH processing.

Figure 2-1. Locations of the 30 collocated National Data Buoy Center (NDBC) buoys.

Figure 2-2. Buoy T_z^B and altimeter T_a^A data when the wind speed is lower (**a**) or higher (**b**) than 5 m·s^{-1}. In the right-hand panel, the blue (red) plots indicate data for which the wind speed is higher (lower) than 10 m·s^{-1}. The regression lines estimated by the orthogonal distance regression (ODR) method are plotted by the dashed (0–5 m·s^{-1}), broken (5–10 m·s^{-1}), and solid (>10 m·s^{-1}) green lines.

Figure 2-3. Buoy T_a^B and altimeter T_a^A when the wind speed is lower (**a**) or higher (**b**) than 5 m·s^{-1}. In the right-hand panel, the blue (red) plots indicate data for which the wind speed is higher (lower) than 10 m·s^{-1}. The regression

lines estimated by the ODR method are plotted by the dashed (0–5 m·s^{-1}), broken (5–10 m·s^{-1}), and solid (>10 m·s^{-1}) green lines.

Figure 2-4. Buoy H_s^B and altimeter H_s^A when the wind speed is lower (a) or higher (b) than 5 m·s^{-1}. In the right-hand panel, the blue (red) plots indicate data for the case in which the wind speed is higher (lower) than 10 m·s^{-1}.

Figure 2-5. Buoy MSS^B and altimeter MSS^A when the wind speed is lower (a) or higher (b) than 5 m·s^{-1}. In the right-hand panel, the blue (red) plots indicate data for the case in which the wind speed is higher (lower) than 10 m·s^{-1}.

Figure 2-6. Compensated high-frequency portion of *MSS* for buoys. The red, blue, and black lines represent the equilibrium range, the saturation range, and the total range, respectively.

Figure 2-7. Buoy MSS^{CB} and altimeter MSS^A when the wind speed is lower (a) or higher (b) than 5 m·s^{-1}. In the right-hand panel, the blue (red) plots indicate data for the case in which the wind speed is higher (lower) than 10 m·s^{-1}.

Figure 2-8. Buoy T_a^{CB} and altimeter T_a^A data when the wind speed is lower (**a**) or higher (**b**) than 5 m·s^{-1}. In the right-hand panel, the blue (red) plots indicate data for which the wind speed is higher (lower) than 10 m·s^{-1}. The regression lines estimated by the ODR method are plotted by the dashed (0–5 m·s^{-1}), broken (5–10 m·s^{-1}), and solid (>10 m·s^{-1}) green lines.

Figure 2-9. Amount of data for the 16 data subsets.

Figure 2-10. Scatter plot of T_z^B with T_a^B (blue) or T_a^{CB} (red), together with regression lines (solid and broken lines, respectively). For subsets (**a**) wind speed: 4–5 m·s^{-1} and (**b**) wind speed: 10–11 m·s^{-1}.

Figure 2-11. (**a**) Slope of the regression lines of T_a^B (blue) and T_a^{CB} (red) for 16 data subsets. (**b**) RMSD around the regression lines of T_a^B (blue) and T_a^{CB} (red) for 16 data subsets.

Figure 3-1. Ground track (solid blue line) and footprint (broken blue line) of Jason-2 altimeter over Tsushima in Japan. The shortest distance between tide gauge and altimeter ground track is about 7km. Only the waveforms measured at south side (Red line) of Tsushima are used in order to facilitate validation by tide gauge measurements.

Figure 3-2. (a) Schematic showing the geometrical relationship between altimeter and a high reflector (bright patch) on sea surface. (B) The parabolic shape in the echogram. Δy is the geographical distance between a point y_i with y_0(nearest approach), and Δt represents the round-trip time difference in gate, $\Delta t = t_1 - t_0$ ($1gate = 3.125ns$).

Figure 3-3. (a) Rescaled and realigned along-track waveforms (echogram) measured by Jason-2 altimeter over Tsushima islands in Japan (pass 36) on 2009.09.22 (cycle 22). The shading area (black patch) represents the land. Each column of the echogram represents an individual waveform at a given latitude and the rescaled power is represented by color. (b) Marked pixels of the echogram with largest 2% by Step 1 in the first loop and the parabola shape used for detection. (c) Four parabolas are detected and masked.

Figure 3-4. (a) Dash lines represent the actual measured 34.2ºN (red point in Figure 3-5a). Solid lines represent the fitted waveform using Brown model. (b) The same as (a) but for the masked waveform.

Figure 3-5. The annular altimeter footprint (draw for every five gates) for the waveform measured at 34.2ºN (red point as shown in Figure 3-3a) over Tsushima islands in Japan (pass 36) on 2009.09.22 (cycle 22).

Figure 3-6. The same as Figure 3-4 but for the compensated waveform measured at 34.2ºN as shown in Figure 3-5 (red point as shown in Figure 3-3a).

Figure 3-7. Along-track SSH derived from pass 36 cycle 22 of Jason-2 data over Tsushima islands for three different methods. Black is the result of SGDR product, blue is the result of ALES product and red is the result of this study.

Figure 3-8. Correlation coefficient (CC) (a) and Root mean square difference (RMSD) (b) of sea surface height anomaly (SSHA) derived from tide gauge and altimeter measurements for three different methods. Black is the result of SGDR product, blue is the result of ALES product and red is the result of this study.

Figure 3-9. Comparison of SSHA time series derived from ALES retracker (blue) and this study (red) at 34.11ºN with tide gauge measurements (green).

List of Tables

Table 1-1. The main technical parameters of Poseidon-3 altimeter and orbit of Jason-2 altimeter.

Table 1-2. Result for the T_z two-piece model proposed by Mackay et al. (2008).

Table 2-1. Correlation coefficient (CC), bias, slope of the regression line, and root mean square difference (RMSD) around the regression line for T_a^A vs. T_z^B and T_a^A vs. T_a^B for various ranges of wind speed. All CC are significant at the 99.9% confidence level.

Table 2-2. Correlation coefficient (CC), bias, slope of the regression line, and root mean square difference (RMSD) around the regression line for T_a^A and T_a^{CB} for various ranges of wind speed. All CC are significant at the 99.9% confidence level.

1. Introduction

Radar satellite altimetry is now a mature discipline over the open ocean. Since the Topex/Poseidon mission started from 1992, radar altimeters have been provided global, real time, all-weather accurate measurements of sea surface exceed 30 years. The satellite altimeter products have been beneficial to a wide range of scientific questions, including global ocean circulation monitoring, long-term sea level rise and operational oceanography, etc. (Vignudelli et al., 2011).

The fundamental parameters measured by radar altimeters are the satellite height above the sea surface (known as "range"), the significant wave height (SWH, H_s) and the backscatter power (σ_0) (related to the surface wind). In addition, Challenor and Srokosz (1991) proposed that wave period could be derived from altimeter H_s and σ_0 measurements. As the statistical character parameters describing the sea state, the wave height and period are important in theoretical research on ocean wave, in coastal and offshore engineering, and other applications. Traditionally, wave parameters are often obtained from sea wave frequency spectra measured by in situ buoys. However, the use of buoys is restricted to primarily coastal regions and, hence, cannot provide information on global ocean wave conditions. On the other hand, the altimeter measurements of H_s are widely accepted to be of comparable accuracy to that of in situ measurements (e.g., Krogstad and Barstow, 1999; Challenor and Cotton, 2002). In recent years, many altimeter wave period retrieval models have been proposed (Davies et al., 1997; Hwang et al., 1998; Sarkar et al., 1998; Gommenginger et al., 2003; Quilfen et al., 2004; Kshatriya et al., 2005; Mackay et al., 2008; Govindan et al., 2011; Badulin, 2014). However, these models perform worse in low-wind conditions than in high-wind conditions.

In contrast to the open ocean, the radar altimeter data gathered over the coastal zone (particularly in the last 10 km from the coastline) are always flagged as "bad" due to the issues of land contamination in the footprint and intrinsic difficulties in the geophysical corrections. In the last couple of years, significant research has been carried out to overcome these problems and extend the capabilities of current and future altimeters to the coastal zone, with the aim of integrating the altimeter-derived measurements of sea level, wind speed, and significant wave height into coastal ocean observing systems. (Cipollini et al. 2009). Although the application of new techniques (like Ka-

band and Delay-Doppler) will enhance the capabilities of coastal altimetry, the archived coastal altimetry data of conventional pulse-limited radar altimeters would be invaluable for studies of coastal oceanography, such as coastal currents and sea level change et al. In this thesis, two issues on waveform retracking are studied and described in separated parts Ⅰ and Ⅱ; namely, wave period retrieval and waveform retracking over coastal zone, respectively.

This chapter is organized as follows: fundamental altimeter waveform theory is introduced in Section 1.1; an overview of altimeter wave period retrieval is presented in Sections 1.2; the issues of land contamination effect on coastal waveforms is introduced in Section 1.3; in Section 1.4, the objectives and organization of this thesis are introduced.

1.1 Altimeter Waveform Theory

1.1.1 Altimeter Waveform

As the Jason-2 altimetry data is used in this thesis, the Poseidon-3 altimeter of Jason-2/OSTM mission is used to introduce the fundamental waveform theory of pulse-limited radar altimeter. Jason-2/OSTM takes over and continues Topex/Poseidon and Jason-1 missions in 2008. It carries a Poseidon-3 altimeter for a high-accuracy altimetry mission. The main technical parameters of Poseidon-3 altimeter and orbit information are listed in Table 1-1. Poseidon-3 is a radar altimeter that emits pulses at two frequencies (13.6 and 5.3 GHz, the second frequency is used to determine electron content in the atmosphere) and analyzes the return signal reflected by the surface. Moreover, Poseidon-3 is equipped with an open-loop tracking technique for which a Digital Elevation Model (DEM) has been developed. The altimeter's onboard memory contains the elevation values of areas overlayed by the ground tracks. These data, combined with Doris, are used to position the radar echo receiving window in advance, in order to anticipate the contrasts of the topography and to give priority to measurements over water. This technique prevents the altimeter from losing track as sometimes occurs with a conventional tracking loop, and enables measurements to be acquired close to the shoreline.

Table 1-1. The main technical parameters of Poseidon-3 altimeter and orbit of Jason-2 altimeter.

Emitted Frequency (GHz)	Dual-frequency (Ku, C) - 13.575 and 5.3
Pulse Repetition Frequency (Hz)	2060 interlaced {3Ku-1C-3Ku}
Pulse duration (microseconds)	105
Bandwidth (MHz)	320 (Ku and C)
Antenna diameter (m)	1.2
Antenna beam width (degrees)	1.28 (Ku), 3.4 (C)
Power (W)	7
Orbit altitude (km)	1336
Orbital velocity (km/s)	7.2

Poseidon-3 altimeters transmit modulated chirp pulses towards the sea at nadir, and then records the echoes which reflected from the rough sea surface over the pulse-limited altimeter ground footprint. These pulses are emitted at regular intervals defined by the Pulse Repetition Frequency (PRF): about 1800Hz for Ku-band pulse (Table 1-1). The acquisition depends on the functioning of the on-board tracker, which adjusts the altimeter observation window in time in order to keep the reflected signal coming from the Earth within the window. In order to reduce geophysical Rayleigh noise (speckle) in individual received echoes and to perform the time tracking, these individual echoes are averaged on-board every 50 ms (20Hz). The power of returned echoes as received by altimeter is registered in a time series and sampled with a 3.125 ns two-way travel time resolution. The received power by altimeter represented in time function is also known as “waveform”. Each resolution cell in a altimeter waveform is called as a ”gate”, and totally 104 gates are given for Jason-2.

As show in Figure 1-1, altimeter transmit a pulse towards a flat sea surface. There is only thermal noise exist in waveform before the pulse reached to the sea. After the leading edge of the pulse strikes the sea surface, the area illuminated by the pulse grows linearly to form a disk until the trailing edge of the pulse reaches the sea surface a time later. The illuminated area is also known as pulse-limited footprint and it represents the region on the sea surface within which specularly reflecting wave facets contribute to the radar return measured by the altimeter. The radius of the footprint circle is controlled by the pulse bandwidth, the altitude of altimeter and SWH. For Jason-2, it increases from about 1km for a flat surface to 5km for a SWH of 10 m (Chelton et al., 1989). Meanwhile, the received power by altimeter sharply rise in this process

and this portion is known as the waveform leading edge. Thereafter, the area illuminated by the pulse becomes an expending annulus spreading on the earth surface. As the illuminated area of these annulus stay constant, thus the power of returned signals that reflected back from these annulus are the same if the sea surface is homogenous, but the received power by altimeter will be exponential decaying accounts for the antenna's gain pattern (Amaroucheet et al., 2004). The decaying area of the waveform is known as waveform trailing edge. The effective footprint of a pulse-limited altimeter is controlled by the pulse bandwidth and by the width of the analysis window. The radius of Jason-2 pulse-limited footprint is about 9.6km for flat surface case.

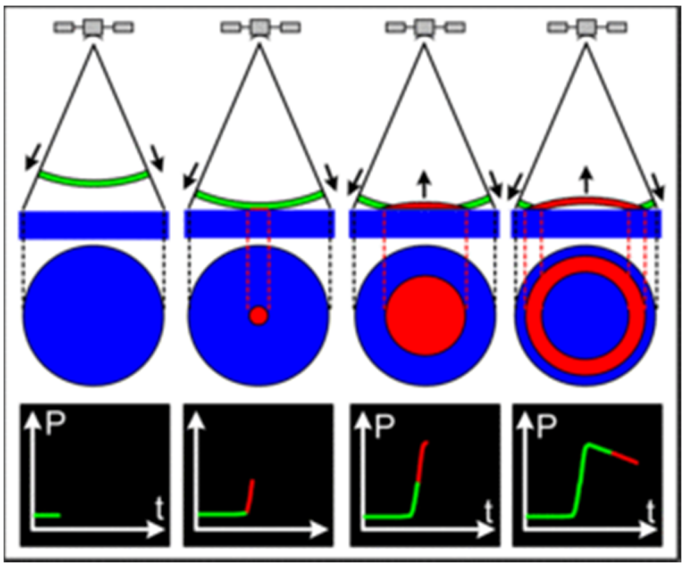

Figure 1-1. The pulse spherically expands to the sea surface at nadir (top); altimeter footprint varies with time (middle); the shape of waveform presents as a fast-rising leading edge and a gradually decaying trailing edge which depending on the antenna beam width. (download from http://www.aviso.altimetry.fr)

1.1.2 Waveform Retracking and Brown model

Waveform parameters are estimated from measured waveforms by a processing step called "waveform retracking" performed on the ground segment. The waveform retracking consists of fitting a model response to the measured waveform. Generally, waveform is spatial integral of instantaneous illuminated area over the pulse-limited footprint. Typical oceanic waveforms has a well-defined shape, with the thermal noise area, the fast-rising leading edge and the gradually decaying trailing edge, and they can be described analytically by the Brown model (Brown, 1977; Hayne, 1980) over the open

ocean. Waveforms on ocean are quite typical of Brown class (as shown in Figure 1-2) since the echo is exclusively reflected by the water. So-called Brown theoretical ocean model is now the standard model over the open ocean. It describes the time evolution of average returned power, $P(t)$, scattered from a rough scattering surface at nadir (namely the waveform) as:

$$P(t) = a_\xi P_u \frac{|1+\mathrm{erf}(u)|}{2} \exp(-v) + T_n \tag{1-1}$$

with:

$$a_\xi = \exp\left(\frac{-4sin^2\xi}{\gamma}\right) \qquad \gamma = \frac{\sin^2\theta_0}{2\cdot\ln 2}$$

$$\mathrm{erf}(x) = \frac{2}{\sqrt{\pi}} \int_0^x e^{-t^2} \mathrm{d}t$$

$$u = \frac{t-\tau-c_\xi\sigma_c^2}{\sqrt{2}\sigma_c} \qquad v = c_\xi\left(t-\tau-\frac{c_\xi\sigma_c^2}{2}\right)$$

$$c_\xi = b_\xi a \qquad b_\xi = \cos(2\xi) - \frac{\sin^2(2\xi)}{\gamma} \qquad a = \frac{4c}{\gamma h\left(1+\frac{h}{R_e}\right)}$$

$$\sigma_c^2 = \sigma_p^2 + \sigma_s^2 \qquad \sigma_s = \frac{H_s}{2c}$$

where c is the speed of light, h is the satellite altitude, R_e is radius of the Earth, ξ is the antenna mispointing (off-nadir) angle, θ_0 is the antenna beam width, τ is the Epoch with respect to the nominal tracking reference point, σ_c is the rise time of the leading edge (depending on a term linked to and on the width of the radar point target response), P_u is the amplitude of the returned signal and T_n is the thermal noise level.

From the waveform retracking using Brown model, several parameters can be deduced:

- Epoch (τ): this gives the time delay between the waveform nominal tracking point (estimated by the on-board tracker, gate 32 for Jason-2) and the retracked waveform mid-point. The distance between satellite altimeter and mean sea surface (*range*) can be derived as follows:

$$\mathrm{range} = \mathrm{tracker\_range} + \frac{c}{2} * \mathrm{Epoch} \tag{1-2}$$

  where c is the speed of light, the tracker_range(all instrument corrections have been included) can be derived from the round-trip time corresponding to the nominal tracking point.

- Amplitude (P_u): the power of returned signal depends upon the scattering character of the sea surface, the transmit power of radar system, the mispointing angle ξ of antenna, and two-way attenuation by the intervening atmosphere. Note that, in order to operate the altimeter electronics within the linear response region of all receiver stages, an Automatic Gain Control (AGC) has been implemented in the electronics package. Therefore, the amplitude of waveforms do not represent the actual sea surface roughness. This can be converted to backscatter coefficient, σ_0, by multiple a scale factor (in linear power units) related to instrument parameter, satellite geometry and AGC etc.(Roca et al., 2000).

$$\sigma_0 = \sigma_0\_scale + 10log_{10}(P_u) \quad (1\text{-}3)$$

  where σ_0_scale is the scaling factor for σ_0 evaluation (dB). Generally, wind speed has inverse relationship with σ_0.

- Rise time of leading edge (σ_c): this is also referred to as leading edge slope, depending on a term σ_s linked to SWH, H_s, and on the width of the radar point target response σ_p. For Jason-2, $\sigma_p = 0.513r_t$, r_t is the time resolution (3.125 ns for Jason-2).

$$H_s = 2c\sqrt{\sigma_c^2 - \sigma_p^2} \quad (1\text{-}4)$$

  where c is the speed of light.

- Antenna mispointing angle (ξ): linked to the slope of trailing edge with strong impact on retrieved amplitude, P_u, reducing the apparent backscatter coefficient of the radar antenna (i.e. any deviation from nadir of the radar pointing). This parameter is estimated from the decaying trailing edge of waveform which also referred to as trailing edge slope. In fact, the slope of the waveform trailing edge is due to antenna beamwidth, to mispointing of the antenna, and/or to sea surface specularity (Raney, 2008). As globally Jason-2 platform real mispointing is near to zero, the slope of the trailing edge mainly represents the regions where geophysical effects like sigma0 bloom events and rain cells take place.

- T_n: this is linked to the thermal noise level in real waveform which should be removed from the waveform samples.

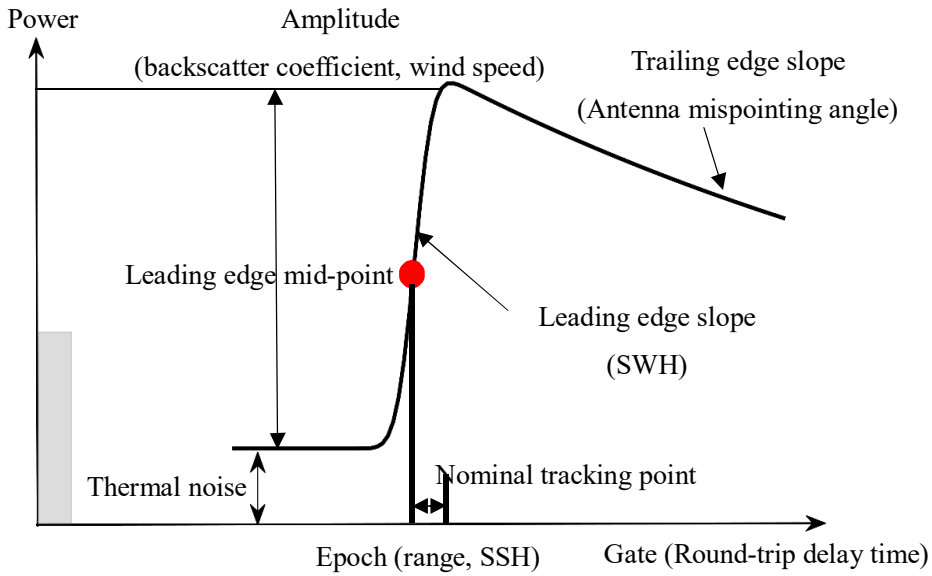

Figure 1-2. Characteristics of typical Brown waveform over the open ocean.

1.2 Overview of Altimeter Wave Period Retrieval Models

As mentioned in Section 1.1, two parameters measured by radar altimeter are related to the sea state, the significant wave height H_s and backscattering coefficient σ_0 which is related to the wind speed u_{10}. It provide the probability of deriving a wave period parameter from the two parameters. In recent years, many altimeter wave period retrieval models have been proposed. These models can be divided into two groups:

- The first one (Hwang et al., 1998; Zhao, 2002) derive a wave period model, $T(H_s, u_{10})$, through the empirical relationship between dimensionless wave parameters based on wind sea theory (Toba, 1972; Hasselmann et al., 1976). These models based on the assumptions of a "saturated" sea condition and negligible swell, and hence, it is only suitable for enclosed seas such as the Gulf of Mexico where swell systems from distance sources are not prominent.
- Most of the models belong to the second group. These models derive a two-parametric wave period model, $T(H_s, \sigma_0)$, from co-located altimeter and buoy data sets with no reference to physics of sea waves (e.g., Davies et al., 1997; Gommenginger et al., 2003; Quilfen et al., 2004; Caires et al., 2005; Kshatriya et al., 2005; Mackay et al., 2008; Govindan et al., 2011). These models are widely used for estimates of wave periods from altimeter data

and show reasonable accuracy (Badulin, 2014). However, these models also perform worse in low-wind conditions than in high-wind conditions.

To date the most accurate model proposed is that of the Mackay et al. (2008). They proposed a two-piece altimeter wave period model which is divided according to σ_0, and then performed this model to six altimeters. As listed in Table 1-2, this model produces root mean square errors (rmse) for the estimation of T_z of approximately 0.53 s for high-wind conditions, but the precision deduced to 0.86s for low-wind conditions.

Note, however, that the wave period determined by altimeters' H_s and σ_0 measurements is referred to as the geometric mean wave period T_a (Challenor and Srokosz, 1991), and is defined differently from the zero-crossing wave period T_z, which could cause a systematic discrepancy in the comparisons. Therefore, in Part I of this thesis, the geometric mean wave period directly calculated from buoy wave spectra is compared with the geometric mean wave period calculated from altimeter measurements.

Table 1-2. Result for the T_z two-piece model proposed by Mackay et al. (2008).

	N	δ	$\sigma_0 \leq \delta dB$		$\sigma_0 \geq \delta dB$		Overall	
	sample number	(dB)	Bias (s)	rmse(s)	Bias(s)	rmse(s)	Bias(s)	rmse(s)
TOPEX	8983	12.87	0.0009	0.54	0.0002	0.87	0.0007	0.59
POSEIDON	500	12.81	0.0003	0.55	0.0358	0.88	0.0015	0.60
JASON	3980	12.95	0.0001	0.53	0.0028	0.90	-0.0001	0.59
ERS-2	8283	12.39	-0.0007	0.54	0.0004	0.83	-0.0008	0.59
ENVISAT	2918	12.29	0.0000	0.50	0.0048	0.85	0.0002	0.56
GFO	6069	12.88	0.0008	0.51	0.0014	0.83	0.0006	0.56
		Mean	0.0003	0.53	0.0068	0.86	0.0004	0.58

1.3 Altimeter Waveform in the Coastal Zone

1.3.1 Land Contamination Effect on Coastal Altimeter Waveform

Over an ocean surface, altimeter waveform has a characteristic shape that can be described analytically by the Brown model. While the waveforms are corrupted when altimeters proximity to the coastal zone, where the reflective surfaces over the altimeter footprint are not homogeneous. The corrupted waveforms deviate from the theoretical open ocean shape and make the accurate retrieval of the parameters more difficult (Gommenginger et al. 2011).

Figure 1-3 is an example of a time series of Jason-2 altimeter waveforms

(hereafter referred as to echogram) over Tsushima in Japan. The top subplot of Figure 1-3 is the raw echogram. Each column of the echogram represents an altimeter waveform, the color represents the power of each echo. As an AGC has been implemented in the electronics package to operate the altimeter electronics within the linear response region of all receiver stages, the power cannot represent the actual sea surface roughness. Moreover, since land-to-sea and sea-to-land transitions might influence the behavior of the on-board tracker, the midpoint of waveform cannot be maintained at the nominal tracking point by the on-board tracker, gate 32 for Jason-2. The waveforms as shown in the bottom subplot are re-aligned based only on the tracker movements and re-scaled by the AGC (Tournadre, 1998). The latter subplot more realistically reflects the scattering intensity of sea surface along track. Figure 1-4 depicts the ground track of Jason-2 altimeter over Tsushima in Japan.

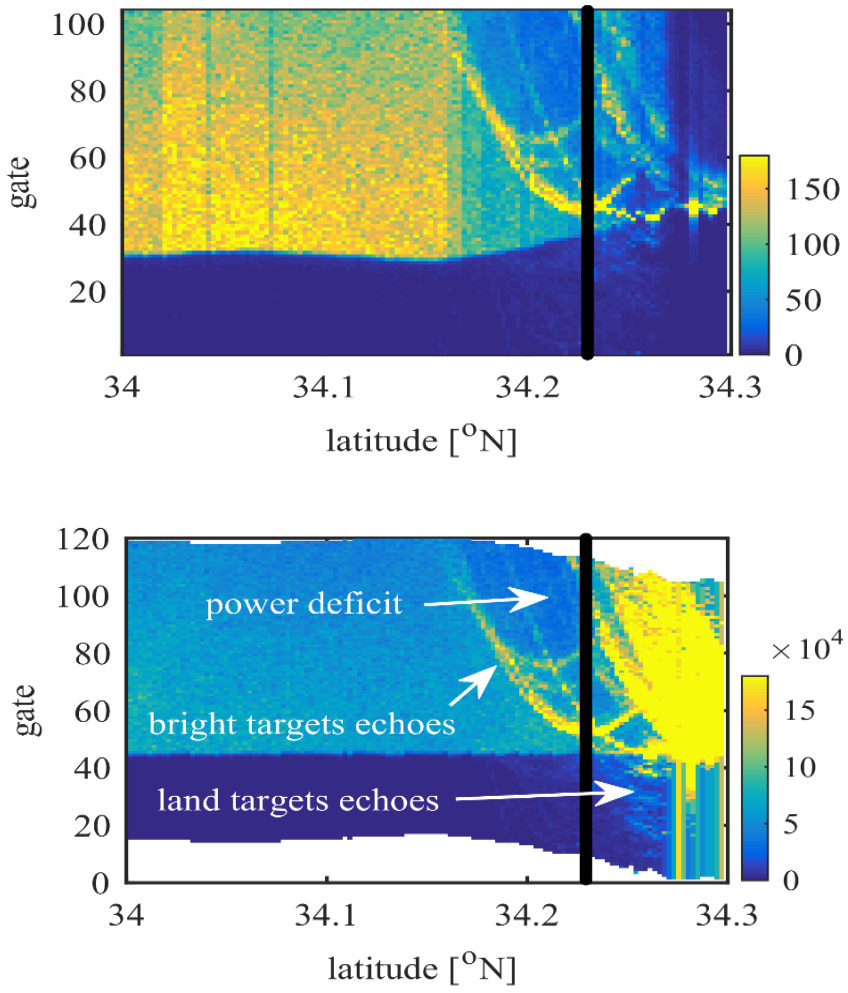

Figure 1-3. Top: Raw echogram of Jason-2 over Tsushima (pass 36) on 2009.09.22 (cycle 45). Bottom: Re-scaled and re-aligned echogram corresponding to the top subplot. Black line represent the coastline.

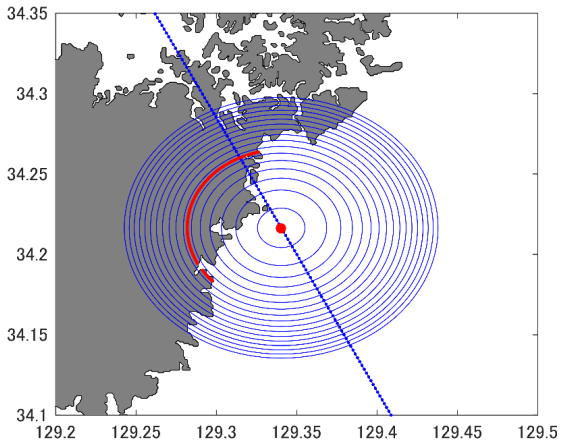

Figure 1-4. Blue line is the ground track of Jason-2 altimeter over Tsushima (pass 36) on 2009.09.22 (cycle 45). Circles represent the pulse-limited altimeter footprint at the red point. The land area (red line) in the footprint lead to the power deficit of waveform trailing edge. The sea surrounded by land always present as "calm water" and seriously corrupt the shape of waveform.

As shown in Figure 1-3, it is obviously that the waveforms are corrupted over the coastal zone. The reasons caused waveform corruption can be divided into three types as follows:

1) Corrupted by the reflection from the targets located above sea level (main lobe or side-lobes), e.g. artificial structures. As the target located above the sea level, it can give an echo even located far from satellite nadir. As shown in Figure 1-5, according to the study of Tournadre (1998), a point target of height 100m above sea level located at distance 17km from the satellites nadir will give an echo at the tail of Jason-2 altimeter waveform trailing edge. However, because the power of the returned signals from these targets generally weak and hence usually only can be seen when they appeared at the thermal noise area.

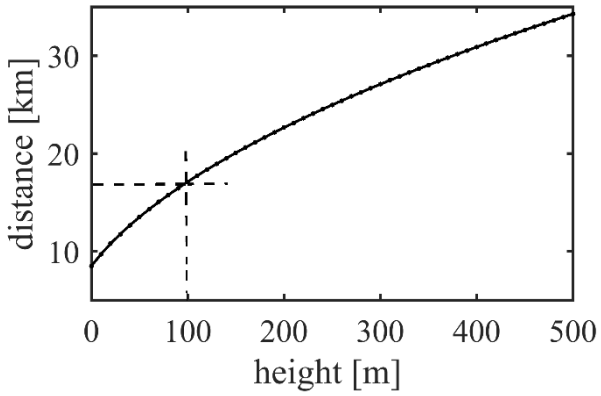

Figure 1-5. Relationship between the height and distance to satellite nadir of a point target which returns could be received by Jason-2 altimeter.

2) Land area located in the altimeter footprint decrease the effective sea surface area and cause the power deficit of waveform trailing edge exceeding the normally decaying caused by antenna pattern (Gómez-Enri et al., 2010). As shown in Figure 1-4, the blue circles represent the annular altimeter pulse-limited footprints. As the land exist in the footprint (red line), the sea surface only accounted for about two third of the area of corresponding annulus.

3) Oceanic surface may have anomalous profiles, particularly, the semi-closed seas always present as bright targets in the radar signal, which also known as "calm water" (Gómez-Enri et al., 2010). The echoes reflected from a bright target such as calm water present as a parabolic shape in the echogram. Two of the predominant coastal waveform classes are quasi-specular and multi-peak echoes (Idris and Deng, 2012, Class 12 and 21 in Figure 1-7). They are both connected with the presence of calm water. Figure 1-6 shows the relationship between the size of calm water and their trajectories on the waveform echogram. For the small size case, which the diameter of calm water is 2km, the calm water behaves like point target and presents as a parabola on the echogram. The parabolic signature which caused by semi-closed sea as shown in Figure 1-3 belong to this kind of situation. Waveforms can be correctly retracked after removing the corrupted echoes along the parabola. As the diameter increasing, a "V-shape" signature can be detected on the echograms. When the diameter of calm water is larger than altimeter footprint size, waveforms can be correctly retracked but with a negative mispointing angle at the center of the V-shape pattern. But for the waveforms very close to the edge of "V-shape", only the echoes

around leading edge should be used for retracking.

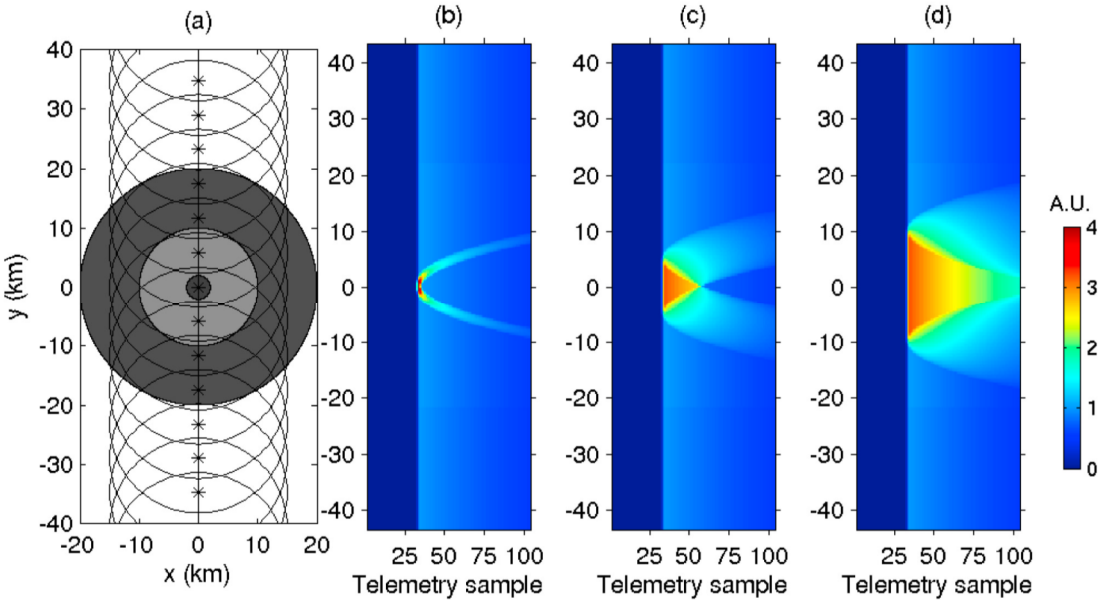

Figure 1-6. Jason altimeter echo waveform in presence of circular slicks of 2 and 10 km radius and 10 and 5 dB relative brightness. (a) Schematic diagram showing the slicks (gray circles) and the altimeter footprint (circles, 1 per second). Modeled waveforms for the (b) 2 km radius and 10 dB brightness slick, (c) 10 km radius and 5 dB brightness slick, and (d) 20 km radius and 5 dB brightness slick. The waveform color scale is in arbitrary units (1 correspond to the maximum value of the Brown model). (Tournadre et al., 2006)

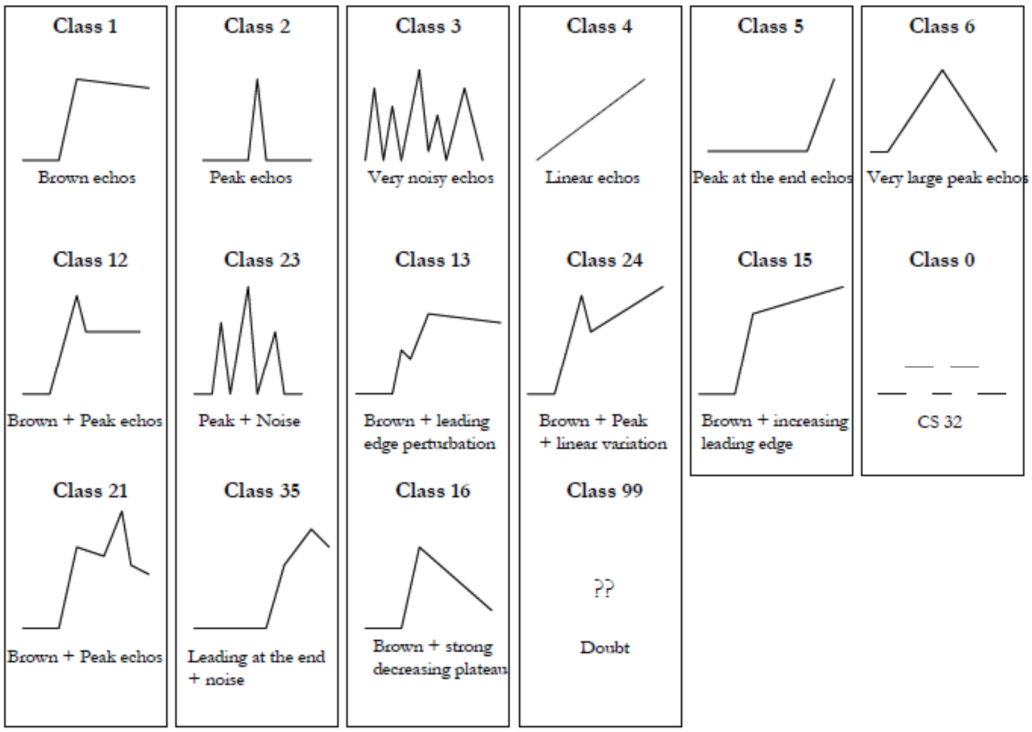

Figure 1-7. Schematic representation of the waveforms classes within the PISTACH processing.

1.3.2 Coastal Waveform Retracking Models

The land contamination on coastal waveforms, particularly evident along the trailing edge pose a real challenge to conventional approach to retrack the coastal waveforms. Many coastal waveform retracking models have been proposed in recent years (Gommenginger et al., 2011). In this thesis, we simply divide these models into two groups according to whether they based on the Brown model based.

Group 1: Non Brown model based models, include the empirical retrackers (Deng and Featherstone, 2006; Hwang et al., 2006; Lee et al., 2008; Bao et al., 2009; Fenoglio-Marc et al., 2009) and the β-parameter retrackers ((Martin et al. 1983). They are originally designed to be used for ice-sea and/or inland waters. In recent years, people also applied them to coastal areas but the precision of retracked SSH is low compared to Brown model even over the open ocean, e.g. about 50cm or 1gate for threshold retracker (Raney, 2010). Moreover, the seamless connect with Brown model requires an accurate quantification of biases assessment.

Group 2: Brown model based models. Mainly include:

- remove the noise (Non-Brown signals) and retrack the full waveform (Quartly, 2010; Tseng et al.; 2014). These studies focused on the peak echo appeared at waveform trailing edge caused by bright targets within the altimeter footprint, but the effect of power deficit due to the existence land area within altimeter footprint have not been discussed as we know.
- the addition of peaks to the Brown model the presence of bright targets (Tourneret et al.; 2010; Halimi, 2012; Idirs and Deng 2012). It is difficult to apply them to multi-peak waveforms, and did not take the power deficit of trailing edge into consideration.
- retrack the "truncated" waveform, namely a sub-waveform around leading edge rather than the full waveform. These models retrack the truncated waveform rather than full waveform in order to avoid the noise appeared at trailing edge which caused by land contamination. (Passro et al.; 2014). The few gates of waveform used for retracking will deduce the precision especially for the backscatter coefficient estimation.

These coastal waveform retracking models have been greatly improved the data acquisition rate over coastal areas. However there are still several

issues remains unresolved. In fact, none of these models can adapt to any coastal zones and any sea conditions. It is difficult to identify whether a signal is contaminated from a single waveform, on the other hand, the bright targets returns will leave a parabolic trajectory on the waveform echogram.

1.4 Objectives and Organization of this Thesis

Part Ⅰ: Many altimeter wave period retrieval models have been proposed but all of them lost its precision in low-wind conditions. In these past researches, the in situ buoy measurements are always treated as "true value", but the buoys cannot measure high-frequency waves whose wavelength smaller than buoy size. Therefore, the effect of high-frequency sea waves on wave period retrieval from radar altimeter and buoy data is considered in this thesis.

Part Ⅱ: It is difficult to determine whether an echo is contaminated in a single waveform. Therefore, the sub-waveform retracking methods are always used for retracking coastal waveforms in the past studies, which pursue a sequential point-by-point retracking method for global altimeter data. On the other hand, for a specific sea area of interest, it is more convenient to determine the contaminated echoes in the echogram and modify the corrupted waveforms. In this thesis, we introduce a waveform modification method and then performed it to Jason-2 altimeter waveforms over Tsushima islands in Japan.

Finally, the conclusion is presented in Section 4.

2. PART I : Wave Period Retrieval by σ_0 and SWH

2.1 Introduction

This chapter is organized as follows: the dataset used in the present study is presented in Sections 2.2; the derivation of wave parameters from buoy and altimeter measurements is introduced in Section 2.3. In Section 2.4, the comparison of geometric wave period obtained from buoy (T_a^B) and altimeter (T_a^A) reveals that T_a^B is larger than T_a^A, primarily because buoys missed high-frequency sea waves having wavelengths that are shorter than the characteristic dimension of the buoy. When a wavenumber spectral model is used to obtain the data for high-frequency sea waves, the compensated buoy wave period T_a^{CB} is confirmed to agree well with T_a^A, as described in Section 2.5. In Section 2.6, the difference between zero-crossing wave period T_z and geometric wave period T_a and the effects of high-frequency sea waves are further discussed. Finally, a brief summary is presented in Section 2.7.

2.2 Dataset

Datasets of co-located buoy/altimeter measurements have always been used in the retrieval of wave periods from altimeter observations. The co-located US National Data Buoy Center (NDBC) buoy hourly data and along-track AVISO Geophysical Data Records (GDRs) of Jason-2 altimeter data are used in this study. The dataset covers the duration from July 2008 to December 2014.

NDBC, a component of the National Oceanic and Atmospheric Administration's (NOAA) National Weather Service (NWS), maintains a network of data buoys to monitor oceanographic and meteorological data off U.S. coasts including the Great Lakes. NDBC's non-directional and directional wave measurements are of high interest to users because of the importance of waves for marine operations including boating and shipping. Instead of the NDBC hourly reported wave measurements, the frequency spectra of sea waves and wind speed measurements are used in this study, and all of the wave parameters such as wave height and wave period can be derived from the frequency spectra as described in Section 2.3.

Jason-2 altimeter GDR products provide two parameters of sea state, H_s and σ_0, for every second, and the along-track space resolution is about 7km. A judicious choice of time/space collocation criteria is critical to ensure the quality of the dataset. Through comparisons of altimeter-derived wave height, wind speed and wave period with corresponding measurements from NDBC buoys

in the Gulf of Mexico, Hwang et al (1998) studied the quantitative effect of the spatial lag and time lag on the correlation of the TOPEX altimeter and surface buoy measurements of wind and wave parameters. Results showed that the agreement between altimeter and buoy measurements of wind speed and wave height improve with shorter spatial lags, while time lags of up to 1 hour do not produce significant changes in the key statistics such as the RMS difference and the correlation coefficient. In order to insure a sufficiently large number of valid hits to allow meaningful statistical treatments, the space and time separation criteria between altimeter and buoy measurements were set to 50 km and 30 min, respectively. Moreover, as the spatial resolution along ground track of Jason-2 is 7km, only the median of the altimeter measurement within 50 km of the buoy was used to reduce the random sampling variability as recommended by Gower (1996).

Considering the 50km space lag between the co-located buoy/altimeter measurements and sea waves begin to be affected by the ocean bottom when they travel into areas of shallow water, only the buoys located in the open ocean (deeper than 1000 m) were chosen in order to avoid shallow water effects. Finally a total of 30 NDBC buoys were selected (Figure 2-1). After removing some outliers, 4196 pairs of co-located measurements were obtained.

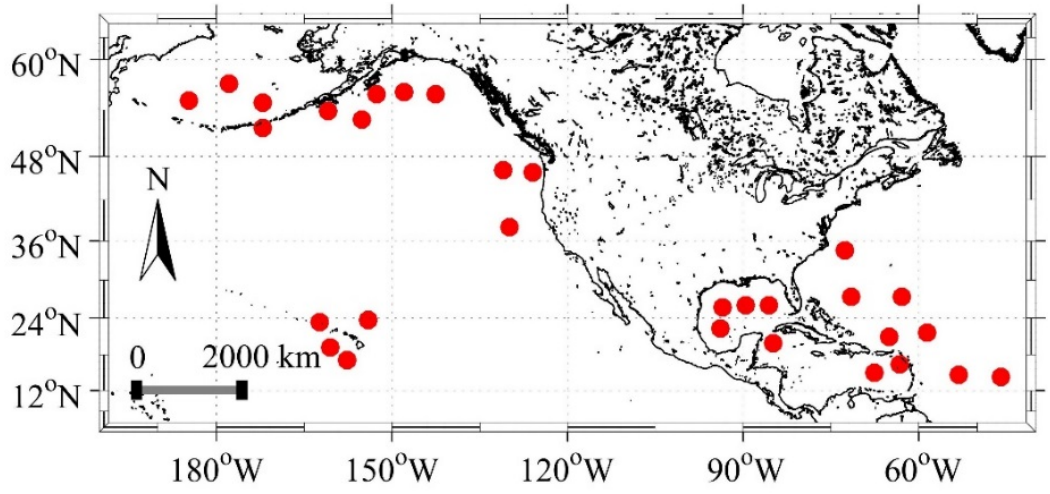

Figure 2-1. Locations of the 30 collocated National Data Buoy Center (NDBC) buoys.

2.3 Rationale of the Retrieval of Altimeter Wave Period

A sea state is the condition of the ocean surface, considered as a stochastic field, that is characterized by statistics such as the wave height, period, and direction-independent wavenumber spectrum $\varphi(k)$ or frequency spectrum $F(f)$, where f is the frequency in Hz and k is the wavenumber. In the case of NDBC buoy measurements, $F(f)$ is determined through a time series of buoy

motion, and all of the basic wave measurements are derived from n-th wave spectral moments, which are defined as:

$$m_n = \int_0^\infty f^n F(f) df, \text{ for } n = \ldots, -3, -2, -1, 0, 1, 2, 3, \ldots \quad (2\text{-}1)$$

Based on the linear theory assumption, the basic wave height and period parameters are calculated as follows (Tucker, 1992):

Significant wave height (H_s):

$$H_s = 4\sqrt{m_0} \quad (2\text{-}2)$$

Average zero-crossing wave period (T_z):

$$T_z = \sqrt{\frac{m_0}{m_2}} \quad (2\text{-}3)$$

Moreover, the crest period T_c is defined as follows:

$$T_c = \sqrt{\frac{m_2}{m_4}} \quad (2\text{-}4)$$

A wave buoy, which is finite in size, is not able to follow waves having wavelengths shorter than the approximate diameter of the buoy, and the corresponding limiting frequency is called the cut-off frequency. In the present study, we use f_l and f_u to represent the lower and upper cut-off frequencies, respectively. For most of the NDBC buoys considered in the present study, f_l is 0.02 Hz, since waves with periods longer than 50 s are practically negligible. Meanwhile, f_u is 0.485 Hz, and thus, based on the deep water dispersion relationship, $f^2 = (2\pi)^{-2} gk$, data for high-frequency sea waves having wavelengths of less than approximately 6.6 m are not captured.

Unlike buoy measurements, radar altimeters cannot capture the spectral information of sea waves. Instead, H_s and σ_0 are directly derived from the one-second averaged time series of the sea surface echo of microwave radar (namely the waveform). We hereinafter use superscripts A and B to indicate altimeter and buoy measurements, respectively. For example, H_s^A and H_s^B represent significant wave height measurements obtained by an altimeter and a buoy, respectively.

For near-nadir incidence radar applications, the backscatter coefficient, σ_0, is commonly considered as being due primarily to specular reflection and is inversely proportional to the wind stress. For an isotropic rough surface having a Gaussian distribution, the backscatter coefficient due to specular reflection can be expressed as follows (Barrick, 1974):

$$\sigma_0 = \frac{|R(0)|^2}{MSS^{\mathrm{A}}} \sec^4\theta \exp\left(-\frac{\tan^2\theta}{MSS^A}\right), \quad (2\text{-}5)$$

where σ_0 is the backscatter coefficient in natural units, $|R(0)|^2$ is the Fresnel reflection coefficient at normal incidence characterizing the surface reflectivity, MSS^A is the filtered mean square slope (MSS) of the sea surface measured by altimeter, and θ is the radar incidence angle. In the present study, we use $|R(0)|^2 = 0.61$ (Klein and Swift, 1977), and MSS^A represents the portion of surface roughness elements having length scales greater than the diffraction limit, 3λ, where λ is the radar wavelength (Vendemark et al., 2004), namely greater than 6.6 cm for the 2.2 cm Ku-band radar altimeter. For normal incidence radar altimeters, $\theta = 0$, equation (2-5) can be simplified as follows:

$$\sigma_0 = \frac{|R(0)|^2}{MSS^A}. \tag{2-6}$$

The MSS can be obtained by integrating the slope spectrum, $\varphi(k)k^2$, as (Phillips, 1977):

$$MSS = \int_0^\infty \varphi(k)k^2 dk, \tag{2-7}$$

where $\varphi(k)$ is the direction-independent wavenumber spectrum. Using the deep water dispersion relationship and the Jacobian operator (Holthuijsen, 2007), the MSS can be expressed using the direction-independent frequency spectrum, $F(f)$, as follows (Li et al., 2003):

$$MSS = \int_0^\infty \frac{(2\pi f)^4}{g^2} F(f) df = \frac{16\pi^4}{g^2} m_4, \tag{2-8}$$

where m_4 is the fourth spectral moment, and g represents the acceleration of gravity.

Based on Equations (2-3) and (2-4), the geometric mean wave period T_a can be defined as follows (Challenor and Srokosz, 1991):

$$T_a = \sqrt{T_z \times T_c} = \left(\frac{m_0}{m_4}\right)^{0.25}. \tag{2-9}$$

For buoy measurements, T_a can be obtained directly from spectral moments by:

$$T_a^B = \left(\frac{m_0^B}{m_4^B}\right)^{0.25}. \tag{2-10}$$

Based on Equations (2-2), (2-6), (2-8), and (2-9), T_a can be derived from altimeter measurements by (Davies et al., 1997):

$$T_a^A = \left(\frac{m_0^A}{m_4^A}\right)^{0.25} = \frac{\pi}{\sqrt{g|R(0)|}} \times (\sigma_0 (H_s^A)^2)^{0.25}. \tag{2-11}$$

Therefore, both altimeter and buoy measurements can be used to obtain T_a. Note that this formulation is very similar to the model proposed by Gommenginger et al (2003), which used heuristic arguments to show that the wave period can be retrieved using a linear relationship, namely $T \sim \left(\sigma_0 {H_s}^2\right)^{0.25}$.

Note, however, that the wave period determined by altimeters' H_s and σ_0 measurements is referred to as the geometric mean wave period T_a, and is defined differently from the zero-crossing wave period T_z, which could cause a systematic discrepancy in the comparisons. Therefore, in the next chapter, the geometric mean wave period T_a^B directly calculated from buoy wave spectra is compared with the geometric mean wave period T_a^A calculated from altimeter measurements.

2.4 Comparison of Geometric Mean Wave Periods Determined from Buoy and Altimeter Data

In this study, we use various statistics to quantify the comparisons, namely the correlation coefficient (CC), bias, slope of the regression line, and root mean square difference (RMSD) around the regression line. First, the wave periods T_z^B and T_a^A, which are defined differently, are compared, as shown in Figure 2-2. Referring to the two-piece wave model proposed by Mackay et al. (2008), the plots are divided according to the wind speed conditions. The geometric mean wave period determined by altimeter data T_a^A is positively correlated with the zero-crossing wave period determined by buoy data T_z^B under all wind conditions. However, as the wind speed decreases, the CC and RMSD around the regression line estimated by the orthogonal distance regression (ODR) method (Boggs and Rogers, 1990) become small and large, respectively, as shown in Table 2-1. In addition, T_a^A is always significantly shorter than T_z^B. This could be due to either the difference in the definitions of the wave periods or the observation methods, or even due to improper choice of the $|R(0)|^2$ constant.

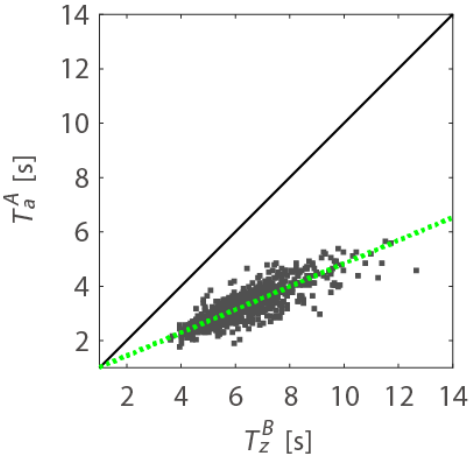

(a)

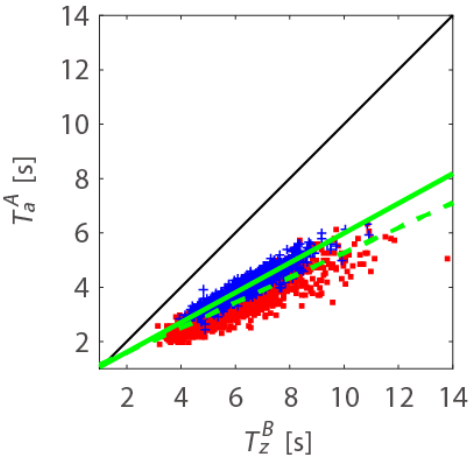

(b)

Figure 2-2. Buoy T_z^B and altimeter T_a^A data when the wind speed is lower (**a**) or higher (**b**) than 5 m·s^{-1}. In the right-hand panel, the blue (red) plots indicate data for which the wind speed is higher (lower) than 10 m·s^{-1}. The regression lines estimated by the orthogonal distance regression (ODR) method are plotted by the dashed (0–5 m·s^{-1}), broken (5–10 m·s^{-1}), and solid (>10 m·s^{-1}) green lines.

Table 2-1. Correlation coefficient (CC), bias, slope of the regression line, and root mean square difference (RMSD) around the regression line for T_a^A vs. T_z^B and T_a^A vs. T_a^B for various ranges of wind speed. All CC are significant at the 99.9% confidence level.

	Wind Speed (data number)	**u ≤ 5 m·s^{-1} (727)**	**5 < u ≤ 10 m·s^{-1} (2683)**	**u > 10 m·s^{-1} (786)**	**Overall (4196)**
T_a^A vs. T_z^B	CC	0.83	0.89	0.94	0.84
	bias ($T_z^B - T_a^A$)	3.1 s	2.5 s	2.3 s	2.5 s
	slope	0.42	0.46	0.55	0.48
	RMSD	0.7 s	0.6 s	0.2 s	0.5 s
T_a^A vs. T_a^B	CC	0.82	0.91	0.93	0.85
	bias ($T_a^B - T_a^A$)	2.1 s	1.5 s	1.4 s	1.6 s
	slope	0.62	0.74	0.79	0.74
	RMSD	0.7 s	0.5 s	0.2 s	0.5 s

Next, the geometric mean wave periods of the buoys T_a^B were directly calculated from wave spectra and were compared with T_a^A, as shown in Figure 2-3. Compared with Figure 2-2, the estimated wave periods T_a^B and T_a^A (defined similarly) result in better agreement than wave periods T_z^B and T_a^A (defined differently). In particular, the slope of the regression lines becomes closer to unity. Nevertheless, a mean bias of 1.6 s ($T_a^B - T_a^A$) and an RMSD of 0.5 s around the regression line remain (Table 2-1).

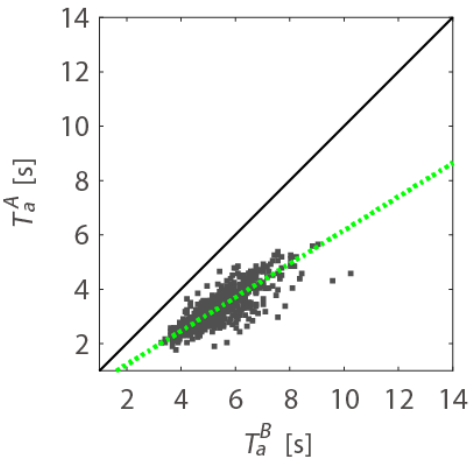

(a)

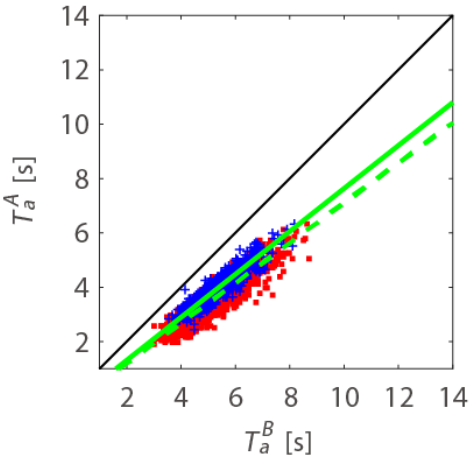

Figure 2-3. Buoy T_a^B and altimeter T_a^A when the wind speed is lower (**a**) or higher (**b**) than 5 m·s⁻¹. In the right-hand panel, the blue (red) plots indicate data for which the wind speed is higher (lower) than 10 m·s⁻¹. The regression lines estimated by the ODR method are plotted by the dashed (0–5 m·s⁻¹), broken (5–10 m·s⁻¹), and solid (>10 m·s⁻¹) green lines.

In order to examine the reason for the remaining discrepancy between T_a^A and T_a^B, H_s and MSS are examined because they are directly related to m_0 and m_4, respectively, which are used in the derivation of T_a. Altimeters are known for their ability to estimate significant wave height, and this was confirmed by the comparison of the present study, even in low-wind conditions. As shown in Figure 2-4, the data of altimeter Hs^A almost perfectly agrees with that of buoy Hs^B, as determined by Equation (2-2), where the CC is 0.98 and the RMSD is 0.2 m.

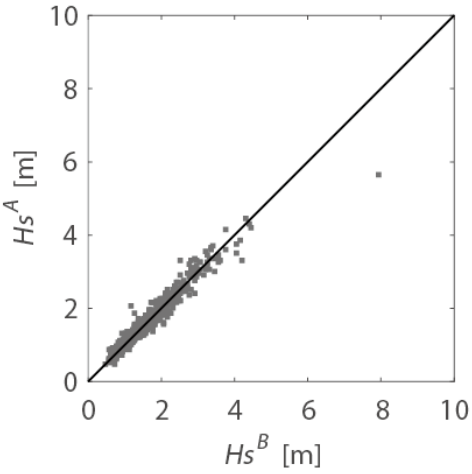

(a)

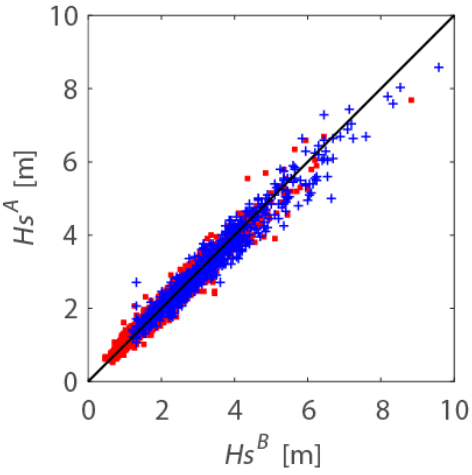

(b)

Figure 2-4. Buoy H_s^B and altimeter H_s^A when the wind speed is lower (a) or higher (b) than 5 m·s^{-1}. In the right-hand panel, the blue (red) plots indicate data for the case in which the wind speed is higher (lower) than 10 m·s^{-1}.

On the other hand, the altimeter MSS^A, which is inversely proportional to σ_0, is significantly larger than MSS^B calculated from the fourth moment of the wave spectra, as shown in Figure 2-5. When the wind speed is higher than 5 m·s^{-1}, MSS^B and MSS^A exhibit a rough linear relationship with the CC exceeding 0.80. In low-wind conditions, the variation range of MSS^B is more limited than that of MSS^A. In other words, MSS^B appears to miss some variations that are observed by the altimeters.

As described in Section 2.3, the buoy cannot measure waves having wavelengths shorter than the characteristic dimension of the buoy. Such a wave would have a larger slope even though its wave height is small, because its horizontal scale is smaller. Therefore, the high-frequency sea waves not captured by the buoy would contribute significantly to the *MSS*, as shown in Figure 2-5, but would contribute less to significant wave height, as shown in

Figure 2-4. In order to confirm this, in the following section, we use a wavenumber spectral model to estimate the *MSS* of the high-frequency sea waves missed by buoys, and the geometric mean wave period is estimated using the compensated buoy *MSS*.

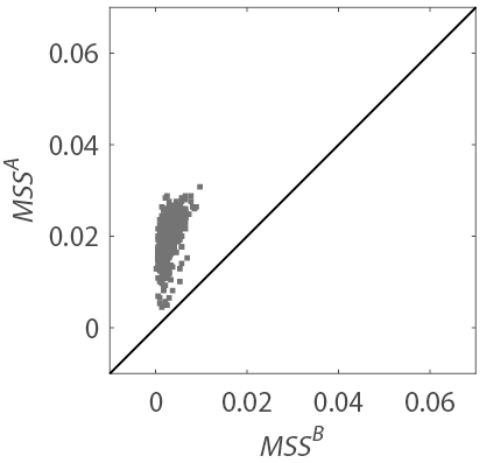

(a)

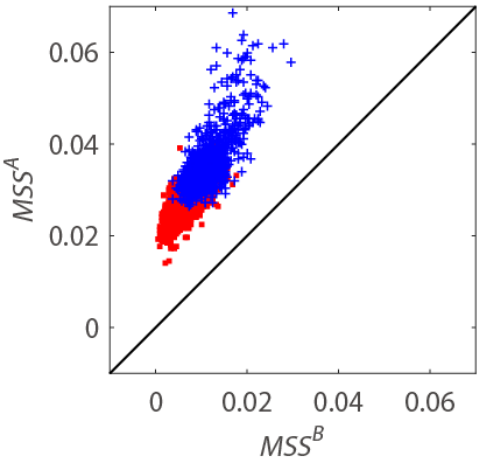

(b)

Figure 2-5. Buoy MSS^B and altimeter MSS^A when the wind speed is lower (a) or higher (b) than 5 m·s^{-1}. In the right-hand panel, the blue (red) plots indicate data for the case in which the wind speed is higher (lower) than 10 m·s^{-1}.

2.5 Compensation of the Mean Square Slope Obtained Using the Buoy Data

As discussed in Section 2.4, the *MSS* is theoretically defined by the direction-independent wavenumber spectrum $\varphi(k)$ in Equation (2-7). Previous studies have shown that the universal form of the equilibrium range spectrum $\varphi(k) \propto k^{-3}$ is no longer rational and should be of the form $\varphi(k) \propto k^{-2.5}$ (Phillips,

1985). Although this form is supported by observations in the rear face region of the spectrum, it cannot be extended to very high wavenumbers. During the last two decades, numerous frequency domain observations have suggested that, in addition to the well-established $k^{-2.5}$ behavior in the rear face region, a fairly abrupt change in spectral slope occurs at approximately $k = 9k_p$, as compared to the slope that follows the k^{-3} law (Hwang et al., 2000), where k_p is the peak wavenumber of wind waves, as defined by $k_p = g/{u_{10}}^2$, and u_{10} is the neutral wind speed at an elevation of 10 m.

Although the proper spectral form remains controversial, the *MSS* of the high-frequency sea waves, MSS^{B-}, is estimated as follows (Hwang and Wang, 2001):

$$MSS^{B-} = \int_{k_l}^{k_u} \varphi(k) k^2 \, dk = \int_{k_l}^{k_1} b u_* g^{-0.5} k^{-0.5} dk + \int_{k_1}^{k_u} B k^{-1} dk, \qquad (2\text{-}12)$$

The first term on the right-hand side of Equation (2-12) represents the equilibrium range spectrum, and the second term indicates the saturation range spectrum, where b = 5.2 × 10^{-2}, u_* is the wind friction velocity, g is the gravitational acceleration, and B = 4.6 × 10^{-2}. The wavenumbers k_l and k_u reflect the integration limits of the low and high wavenumbers, respectively. Here, $k_l = 0.95 \text{ rad} \cdot \text{m}^{-1}$ and $k_u = 100 \text{ rad} \cdot \text{m}^{-1}$ are adopted to estimate the *MSS* missing from the buoy measurements, corresponding to wavelengths approximately from 6 cm (or 3λ of Ku-band radar) to 6.6 m (or the characteristic dimension of the buoy). The wavenumber k_1 divides the wavenumber spectrum into the equilibrium range and the saturation range and is defined as (Hwang and Wang, 2001):

$$k_1 = \left(\frac{B}{b}\right)^2 \frac{1}{C_d} k_p, \qquad (2\text{-}13)$$

where C_d is the drag coefficient for which we adopt the form proposed by Wu (1988).

Figure 2-6 shows the wind speed dependency of MSS^{B-}. As k_p (namely k_1) decreases with the increasing wind speed u_{10}, the first term on the right-hand side of Equation (2-12) decreases to zero when k_1 becomes smaller than k_l, or when u_{10} exceeds approximately 10 m·s^{-1}.

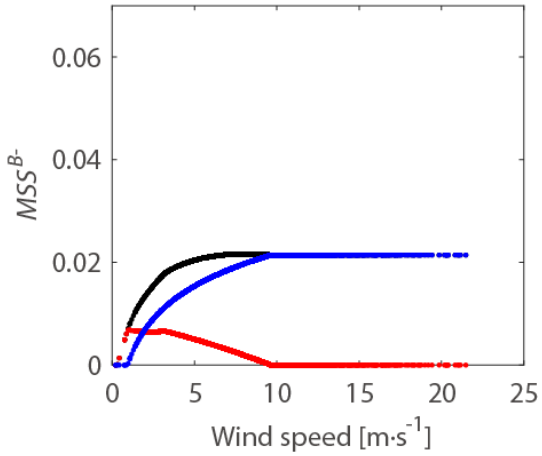

Figure 2-6. Compensated high-frequency portion of *MSS* for buoys. The red, blue, and black lines represent the equilibrium range, the saturation range, and the total range, respectively.

After compensating for high-frequency sea waves, the compensated buoy mean square slope, $MSS^{CB} = MSS^{B} + MSS^{B-}$, shows no obvious bias with altimeter MSS^{A} (Figure 2-7) compared with the uncompensated buoy mean square slope, MSS^{B}, even in low-wind conditions. The CC becomes 0.68 and 0.83 for wind speeds lower and higher than 5 ms^{-1}, respectively.

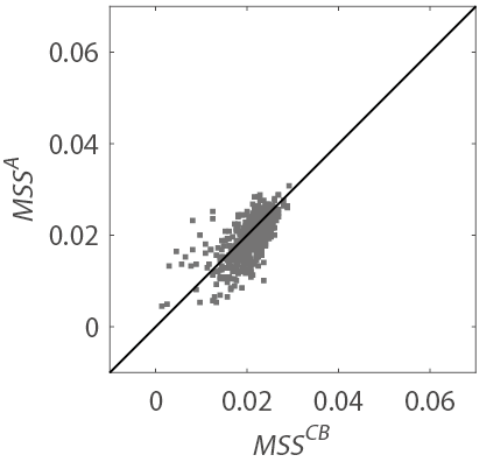

(a)

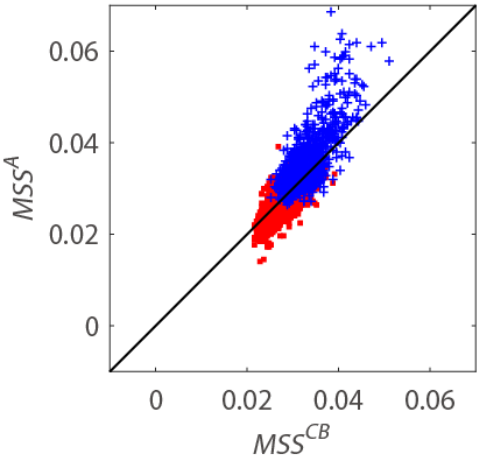

(b)

Figure 2-7. Buoy MSS^{CB} and altimeter MSS^{A} when the wind speed is lower (a) or higher (b) than 5 m·s⁻¹. In the right-hand panel, the blue (red) plots indicate data for the case in which the wind speed is higher (lower) than 10 m·s⁻¹.

The geometric mean wave period for the compensated buoy data, T_a^{CB}, was calculated and compared with altimeter-derived T_a^A. As shown in Figure 2-8, T_a^{CB} is in better agreement with T_a^A than T_a^B (Figure 2-3). The CC, mean bias ($T_a^{CB} - T_a^A$), and RMSD are 0.97, less than 0.01 s, and 0.2 s, respectively, as listed in Table 2-2.

Recall that the significant wave height H_s^B is not affected by the loss of high-frequency sea waves, as shown in Figure 2-4. Since the higher-order moment forces more weight on high-frequency spectra in the integration, the contribution of high-frequency sea waves would become significant for m_4 but negligible for m_0. This suggests that the m_2-based T_z^B would also be affected by the loss of high-frequency sea waves, but in a different manner from the m_4-based T_a^B. Therefore, in the following section, we examine the impact of missing high-frequency sea waves on T_z^B, T_a^B, and T_a^{CB}.

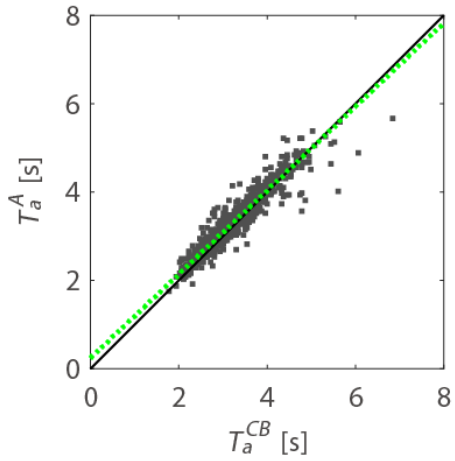

(a)

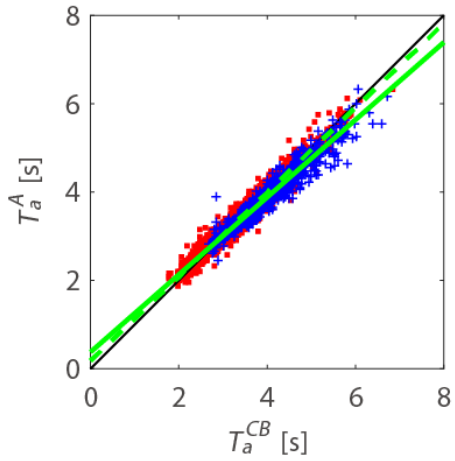

(b)

Figure 2-8. Buoy T_a^{CB} and altimeter T_a^A data when the wind speed is lower (**a**) or higher (**b**) than 5 m·s^{-1}. In the right-hand panel, the blue (red) plots indicate data for which the wind speed is higher (lower) than 10 m·s^{-1}. The regression lines estimated by the ODR method are plotted by the dashed (0–5 m·s^{-1}), broken (5–10 m·s^{-1}), and solid (>10 m·s^{-1}) green lines.

Table 2-2. Correlation coefficient (CC), bias, slope of the regression line, and root mean square difference (RMSD) around the regression line for T_a^A and T_a^{CB} for various ranges of wind speed. All CC are significant at the 99.9% confidence level.

	Wind Speed (Data Number)	u ≤ 5 m·s^{-1} (727)	5 < u ≤ 10 m·s^{-1} (2683)	u > 10 m·s^{-1} (786)	Overall (4196)
T_a^A vs T_a^{CB}	CC	0.94	0.98	0.96	0.97
	bias ($T_a^{CB} - T_a^A$)	−0.1 s	0.0 s	0.1 s	0.0 s
	slope	0.95	0.95	0.89	0.93
	RMSD	0.2 s	0.1s	0.2 s	0.2 s

2.6 Discussion

In order to increase the amount of data for comparison, all data from 30 NDBC buoys are used in this section to calculate T_z^B, T_a^B, and T_a^{CB}, independently from the altimeter data. The data are divided into 16 subsets according to wind speed in intervals of 1 m·s^{-1} (0–1 m·s^{-1}, 1–2 m·s^{-1}, …, 14–15 m·s^{-1}, and higher than 15 m·s^{-1}). As shown in Figure 2-9, the data number of each subset exceeds 15,000 with a maximum of approximately 140,000 samples at 6 to 7 m·s^{-1}.

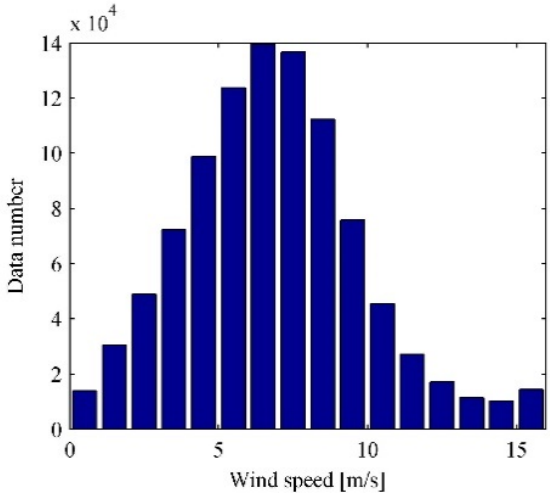

Figure 2-9. Amount of data for the 16 data subsets.

Figure 2-10 shows scatter plots of T_z^B with T_a^B or T_a^{CB} for two wind conditions, together with the regression lines estimated by the ODR method. The slopes of the regression lines of T_a^B are closer to unity for both wind conditions. In other words, the discrepancy between T_z^B and T_a^{CB} is much larger. Moreover, the RMSD around the regression line is much larger for T_a^{CB} in the lower wind condition (Figure 2-10a), whereas, for T_a^B, there is no significant difference between the two wind cases, which suggests that T_a^{CB} is more sensitive to wind speed variation.

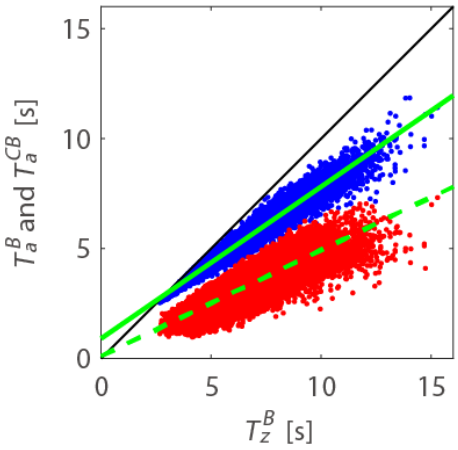

(a)

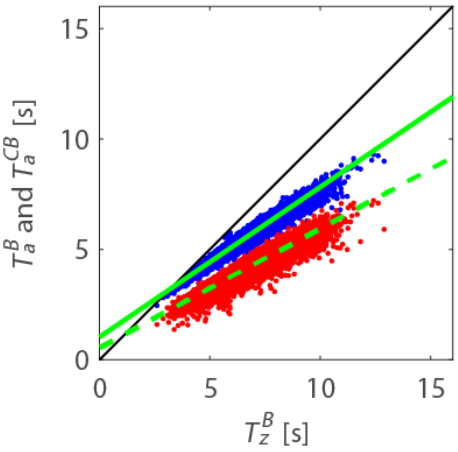

(b)

Figure 2-10. Scatter plot of T_z^B with T_a^B (blue) or T_a^{CB} (red), together with regression lines (solid and broken lines, respectively). For subsets (**a**) wind speed: 4–5 m·s^{-1} and (**b**) wind speed: 10–11 m·s^{-1}.

In order to examine the dependence of the relationship between T_z^B and T_a^B or T_a^{CB} on wind speed, the slope and RMSD of the regression lines were calculated for each of the 16 data subsets, and the results are plotted in Figure 2-11.

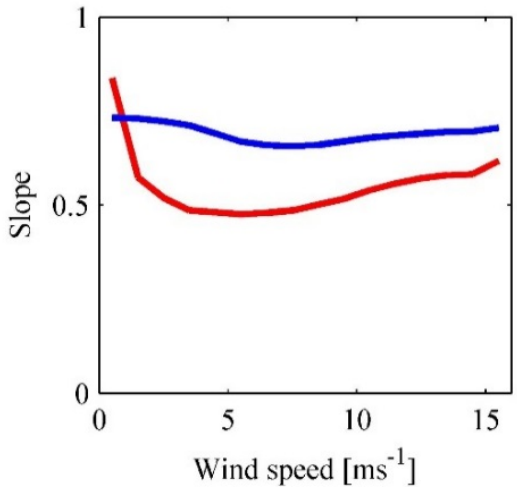

(a)

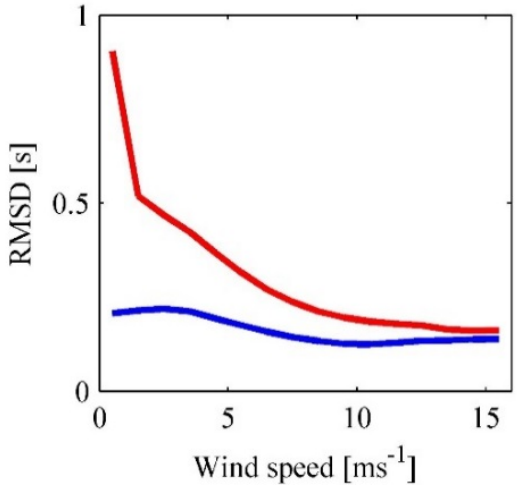

(b)

Figure 2-11. (**a**) Slope of the regression lines of T_a^B (blue) and T_a^{CB} (red) for 16 data subsets. (**b**) RMSD around the regression lines of T_a^B (blue) and T_a^{CB} (red) for 16 data subsets.

For T_a^B, the slope of the regression line varies only slightly with wind speed, and the RMSD remains small. In contrast, for T_a^{CB} (also for T_a^A), the slope of the regression line varies with wind speed, especially in low-wind conditions. The presence of wind waves on background swells shortens T_a^{CB}, resulting in the smaller slope of the regression lines. Since wind waves are more sensitive to wind speeds than swells, the growth of short wind waves decreases the slope values in Figure 2-11a as the wind speed increases until the wind wave spectrum becomes saturated at winds stronger than 5 m·s^{-1}. On the other hand, neither T_a^B nor T_z^A includes short wind waves, and so they are independent of the growth of short wind waves. Therefore, the slope of T_a^B remains approximately constant, as shown in Figure 2-11a.

In addition, because the growth of wind waves depends on not only wind speed but also wind duration, the mean wave periods would diverge even for

the same instantaneous wind speed, especially for T_a^{CB}, which is most sensitive to the growth of wind waves. This would result in a larger RMSD of T_a^{CB} at a lower wind speed and is consistent with Figure 2-11b.

2.7 Conclusions

In previous studies on altimeter wave period retrieval, great efforts were made to establish a relationship between the buoy-derived zero-crossing wave period T_z^B with altimeter-measured significant wave height H_s and the backscatter coefficient σ_0. However, all of the derived algorithms resulted in lower precision in low-wind conditions. Since radar altimeters only provide H_s and σ_0 information about the sea state, that is, the zeroth and fourth wave spectral moments, the geometric mean wave period, $T_a = \left(\frac{m_0}{m_4}\right)^{0.25}$, is estimated from altimeter data and is different from the zero-crossing wave period, $T_z = \left(\frac{m_0}{m_2}\right)^{0.5}$, which is commonly used by in situ buoys. In the present study, the geometric mean wave period T_a^B derived from buoy wave spectra was directly compared with T_a^A.

Higher-order wave spectral moments are more sensitive to high-frequency sea waves. A buoy cannot measure waves shorter than the characteristic dimension of the buoy, so that information of high-frequency sea waves is not captured. Since neither T_z^B nor T_a^B captures the contribution of high-frequency sea waves, they result in a near-linear relationship, independent of wind speed. On the other hand, σ_0 (or the *MSS*) observed by altimeters has high sensitivity to high-frequency sea waves, so that T_a^A is quite different from T_z^B, especially in low-wind conditions.

When the *MSS* due to the missing high-frequency sea waves is compensated, the geometric mean wave period derived from buoy measurements, T_a^{CB}, agrees well with the altimeter-derived period, T_a^A. This suggests that T_a^A observed by altimeters is sufficiently accurate if proper in situ data are compared.

High sensitivity of the *MSS* to high-frequency sea waves is not specific to the radar altimeter measurements, but rather is a common concern with respect to specular reflection. For example, global navigation satellite system reflectometry (GNSS-R) measurements also use the *MSS* at the sea surface, and the retrieved GNSS-R *MSS* was found to be larger than co-located buoy measurements due to the upper cut-off frequency of the buoy (Clarizia, 2012). Therefore, the loss of high-frequency waves by buoys should be carefully taken into consideration when buoy measurements are used to verify remote sensing measurements.

3. PART Ⅱ: Waveform Retracking over Tsushima islands in Japan

3.1 Introduction

As described in Section 1.3, the main factor caused waveform corruption over coastal area is the calm water within altimeter footprint (Idris and Deng, 2012). The reflections from calm water present as redundant peaks in waveform trailing edge. It is difficult to remove these peaky echoes from individual waveforms for the sequential point-by-point retracking method. On the other hand, the parabolic signature of calm water in the echogram can help us to detect and remove these peaky echoes from waveforms. Moreover, the power deficit of waveform trailing edge due to weak land reflection can be compensated in order to obtain more waveform samples for retracking.

The methodology of waveform correction is consist of two steps. First is to remove the redundant peaks caused by calm waters through its parabolic signature in the echogram. Second is to compensate the power deficit of waveform trailing edge. This strategy is performed to Jason-2 altimeter data over Tsushima islands in Japan and results are compared with the results obtained from two other methods, the traditional ocean retracking method (MLE4 for Jason-2 altimeter) which retrack the full waveform and ALES method (Passaro et al., 2014) which retrack a sub-waveform around leading edge, respectively. Tide gauge measurements are used for the validation of data quality.

This chapter is organized as follows: the dataset used in the present study is presented in Sections 3.2; the waveform modification method is introduced in Section 3.3; then the method is performed to Jason-2 altimeter data measured over Tsushima islands in Japan, the results are validated by tide gauge measurements and compared with the classical ocean retracker and ALES retracker as described in Section 3.4; finally, a brief summary is presented in Section 3.5.

3.2 Dataset

The ALES coastal altimetry product of Jason-2 around Tsushima islands in Japan (pass 36 as shown in Figure 3-1) is used in this study. It is an experimental product from the ALES processor included in SGDR-type files alongside the standard products and corrections. The specific description can be found at http://www.coastalt.eu/community. The dataset covers the duration from July

2008 to April 2015. In order to facilitate validation by in situ tide gauge measurements, only the waveforms measured at the south side of Tsushima are used in this thesis.

The full resolution of global self-consistent, hierarchical, high-resolution geography database (GSHHS) (Wessel and Smith, 1996) is used to determine the coastline and estimate the land area located in altimeter footprint.

Hourly tide gauge data obtained from Japan Oceanographic Data Center (JODC) are used to validate the quality of derived along SSH. A temporal interpolation was performed before validation to match up with altimeter measurements. The shortest distance between tide gauge and Jason-2 ground track is about 6km. Moreover, the local wind and rain information obtained from Japan Meteorological Agency (JMA) are used helping us to understand weather conditions.

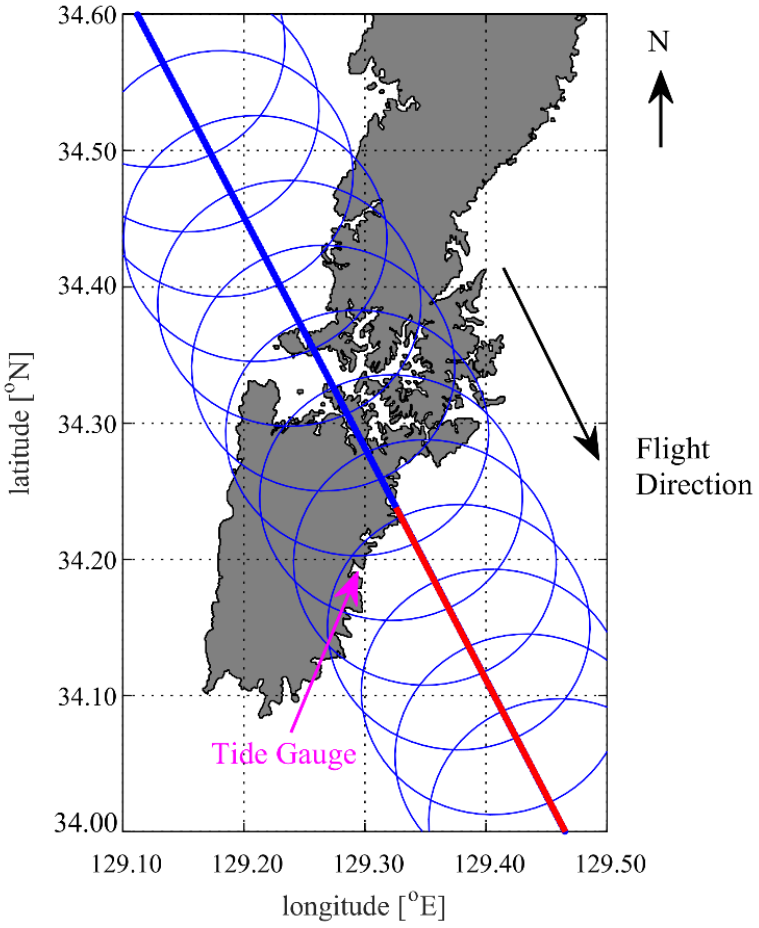

Figure 3-1. Ground track (blue line) and footprint (blue circles draw for every 1 second, radius is 10km) of Jason-2 altimeter over Tsushima islands in Japan. The shortest distance between tide gauge and altimeter ground track is about 6km. Only the waveforms measured at south side (red line) of Tsushima islands are used in order to facilitate validation by tide gauge measurements.

3.3 Waveform Modification Strategy

3.3.1 Detection and Mask of the Redundant Peaks Caused by Calm Waters

Generally, the backscatter coefficient σ_0 of radar altimeters is inversely proportional to the sea surface roughness. In particular, σ_0 will sharply increase when the cm-scale wavelets are absent on the sea surface. The occurrence of unrealistically high values of σ_0 is usually referred to as "sigma-0 blooms" over the open ocean. It shall occur during low wind and sea state conditions or caused by sea surface slicks etc (Tournadre, 2006). Previous studies have shown that the occurrence of unrealistically high values of σ_0 affect almost 5% of the open ocean measurements (Tournadre, 2006; Quartly, 2008).

Different from the open ocean, the calm sea condition is more common over the semi-closed seas. The parabolic signatures caused by semi-closed seas is found in almost all of the 252 cycles of Jason-2 echograms around Tsushima islands. The relative higher reflectivity of semi-closed sea w.r.t. surrounding waters is probably due to the sheltering effect of land. Since coastal waveforms are generally complicated, it is difficult to distinguish whether an echo is corrupted in an individual waveform. In this section, the echoes which are corrupted by calm waters are detected and masked utilizing its parabolic signature in the echogram.

A point target of height δ above sea level located at distance d from the satellite nadir will give an echo at the round-trip delay time t defined by (Tournadre, 2007):

$$\frac{ct}{2} = -\delta + \frac{1}{2}\frac{R_e+H}{R_eH}d^2, \tag{3-1}$$

where c is the speed of light, H is satellite height and R_e is the earth's radius.

For the calm water case, the height δ equals zero. As shown in Figure 3-2a, y_0 represents the location at nearest approach to a high reflector on sea surface, t_0 and d_0 represent the round-trip delay time and geographical distance, respectively. y_i is a point located at distance Δy from y_0, t_i and d_i represent the corresponding round-trip delay time and geographical distance, respectively. Considering the geometric relationship, $\Delta y^2 = {d_i}^2 - {d_0}^2$, Equation (3-1) can be expressed as follows:

$$c\Delta t = \frac{R_e+H}{R_eH}\Delta y^2, \tag{3-2}$$

where Δt represents the round-trip delay time difference, $\Delta t = t_i - t_0$. Equation (3-2) have no relationship with the height of target and its distance

from satellites nadir.

The parabolic shape determined by Equation (3-2) in an echogram is shown in Figure 3-2b. The later axis represents latitude of satellite nadir. The vertical axis represents round-trip delay time in gate, and the sampling resolution is 3.125ns for Jason-2. The vertex of parabola is related to the location of high reflector, and the shape of parabola only determined by the altimeter's orbital and sampling parameters.

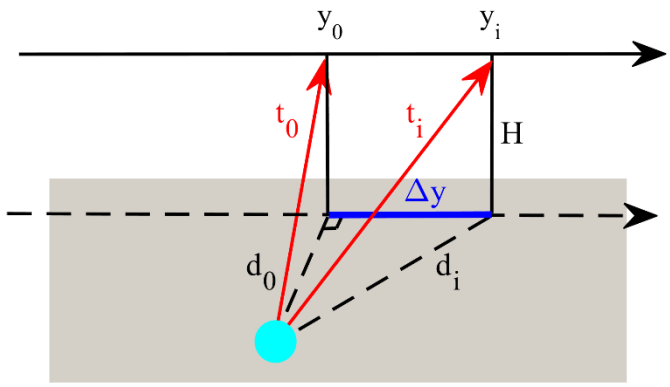

(a)

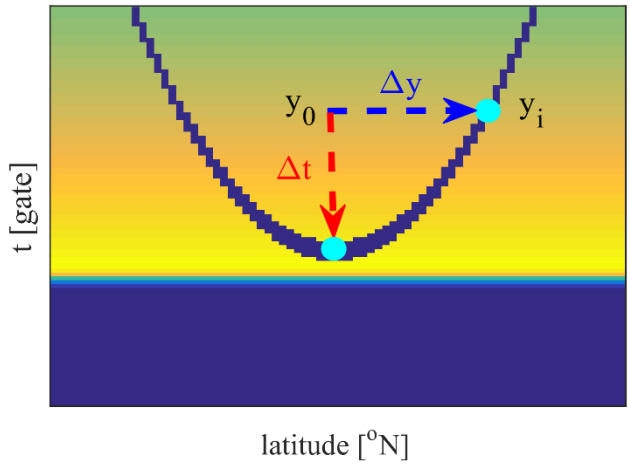

(b)

Figure 3-2. (a) Schematic showing the geometrical relationship between altimeter and a high reflector (bright patch) on sea surface. (B) The parabolic shape in the echogram. Δy is the geographical distance between a point y_i with y_0(nearest approach), and Δt represents the round-trip time difference in gate, $\Delta t = t_1 - t_0$ ($1gate = 3.125ns$).

An iterative method is used to detect the parabolic trajectories in the echogram in the present study. It consists of three steps as follows:

Step1: Mark all pixels of the echogram with largest 2% echoes, but reset these marks for pixels that do not exceed 10dB. The 2% threshold criterion is an empirical value related to the size of study area. The 10dB σ_0 is the lower limit of obvious noises and it is approximately related to 20ms^{-1} wind speed for Jason-2 altimeter.

Step2: Shift the fixed parabolic shape in the echogram both in latitude and gate directions, and count the number N_{mark} of the marked pixels along the parabolic line.

Step3: Find the parabolic shape that provides largest number N_{max}. Mask all pixels (with and without the marks) along this parabolic shape, if N_{max} is larger than 10. Repeat to Step1, until the largest number N_{max} is smaller than 10.

Figure 3-3a depicts the rescaled and realigned echogram echogram measured by Jason-2 altimeter over Tsushima islands (pass 36, cycle 22). It is obviously that four parabolic traces appeared at the trailing edge area of the echogram. Although the echoes located at the tail of parabolas are not significantly strong (weaker than 10dB) due to power decaying of the antenna gain, it is reasonable to remove all of the echoes along the same parabola that are contaminated by a strong point source. Figure 3-3b shows the marked pixels of the echogram with largest 2% by Step 1 in the first loop and the parabola shape used for detection. Four parabolas are detected and masked as shown in Figure 3-3c.

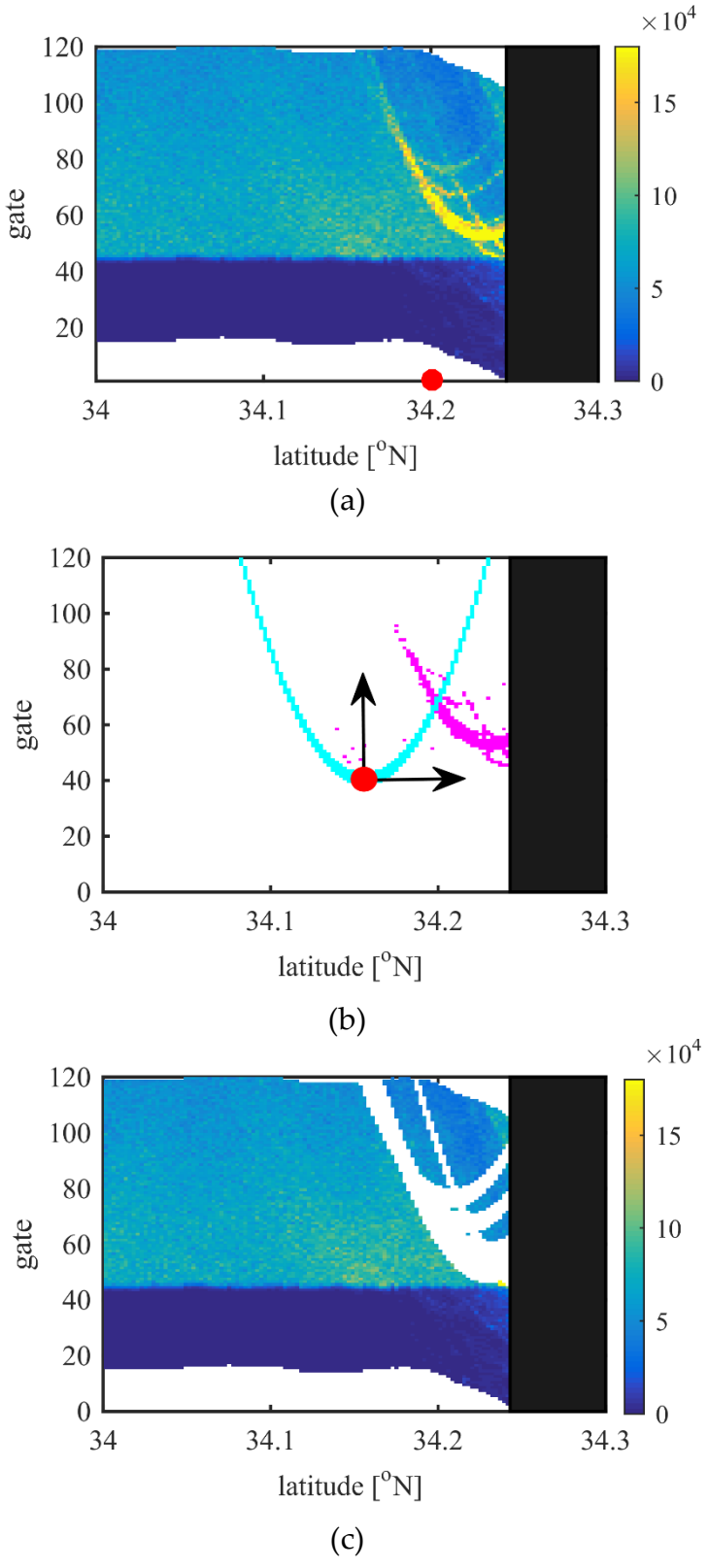

Figure 3-3. (a) Rescaled and realigned along-track waveforms (echogram) measured by Jason-2 altimeter over Tsushima islands in Japan (pass 36) on 2009.09.22 (cycle 22). The shading area (black patch) represents the land. Each column of the echogram represents an individual waveform at a given latitude and the rescaled power is represented by color. (b) Marked pixels of the echogram with largest 2% by Step 1 in the first loop and the parabola shape used for detection. (c) Four parabolas are detected and masked.

The actural and masked waveform as well as their fitted Brown waveform measured at 34.2ºN (red point in Figure 3-3a) are shown in Figure 3-4. Compared to the raw waveform, the leading edge of masked waveform shows well agree with the fitted Brown waveform. However, it is obviously that the masked waveform slightly underestimated σ_0 due to power deficit of waveform trailing edge. In the next section, the power deficit caused by weak land reflection within altimeter footprint is compensated.

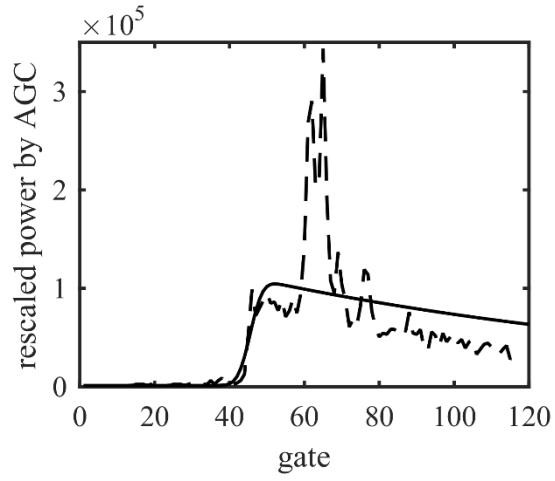

(a)

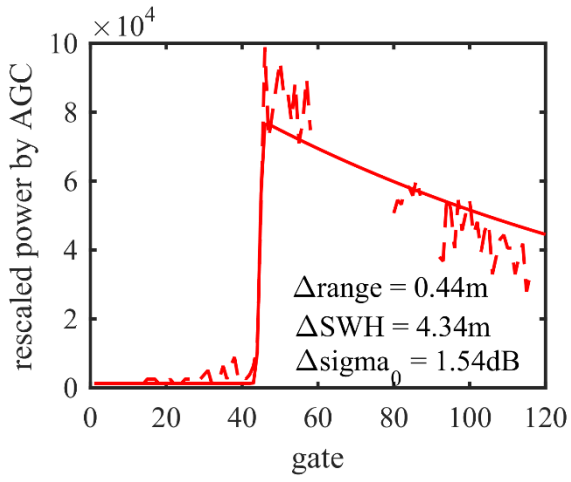

(b)

Figure 3-4. (a) Dash lines represent the actual measured 34.2ºN (red point in Figure 3-5a). Solid lines represent the fitted waveform using Brown model. (b) The same as (a) but for the masked waveform.

In addition to calm water in semi-closed bays, the redundant peaks in waveform trialing edge can also appeare at locations where small-scale sigma0-

bloom events occured. A threshold of σ_0 is always adopted as the bloom detection criterion, e.g. the 15dB and 18dB criterion for the Envisat RA2 data in [14]. The sigma0-bloom events are found in 18 of 252 cycles at the study area by the 18dB threshold criterion. Namely, about 7% of the Jason-2 measurements are corrupted by the sigma0-bloom events. This result is consistent with the study on Jason-1 data (6%) (Tournadre, 2006). The sigma0-bloom effect on waveform retracking is out of the scope of the present study and the 18 cycles data are directly removed from waveform retracking.

3.3.2 Compensation of the Power Deficit of Waveform Trailing Edge

The power of an echo in a waveform is proportional to the area of annular footprint (Figure 3-5a) and controlled by the antenna beam pattern. At the coastal area where land located in altimeter footprint, since the land reflection is very weak, the power is approximately proportional to the ocean area as follows:

$$P(i,j) = P_{ocean}(i,j) + P_{land}(i,j) \approx P_{ocean}(i,j) \sim A_{ocean}(i,j), \quad (3\text{-}3)$$

where i and j are the waveform number and gate number along latitude and gate directions in the echogram, respectively. A_{ocean} represents the equivalent sea surface area located within the corresponding annular footprint. As shown in Figure 6a, the power of waveform trailing edge will fast decay with the decreasing sea surface area in annular footprints. Therefore, a power deficit area can be seen in the echogram as shown in Figure 1-3b and Figure 3-3a.

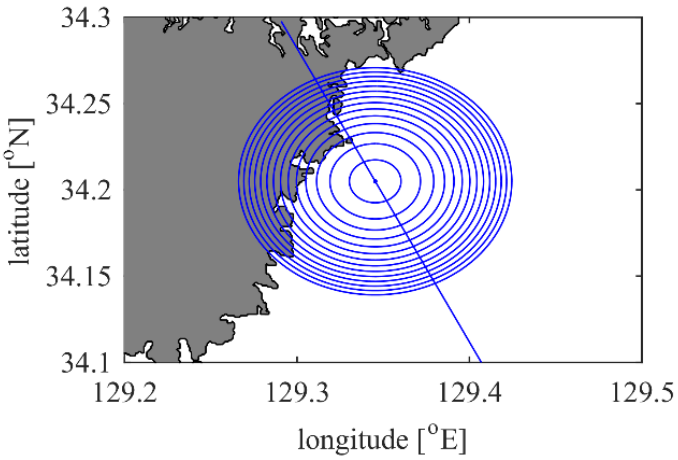

Figure 3-5. The annular altimeter footprint (draw for every five gates) for the waveform measured at 34.2ºN (red point as shown in Figure 3-3a) over Tsushima islands in Japan (pass 36) on 2009.09.22 (cycle 22).

The "illumination hole" in the annular footprint that forms behind the trailing edge of the pulse is a circle with radius and area that expand at the

same rates, and the area of each circle can be calculated followed as (Fu and Cazenave, 2001) by:

$$A_{footprint}(i,j) = \frac{\pi c \Delta t h}{(1+h/R_e)} \ , \tag{3-4}$$

where c is the speed of light, h is the satellite altitude, R_e is radius of the Earth, Δt is the elapsed two-way travel time relative to midpoint of waveform leading edge. In this section, the leading edge detection follows the same as in (Hwang et al., 2006). The difference is that the detection is sequentially implemented from ocean side to coast. For the multi-peak waveforms, the midpoint that nearest to the previous one is selected.

The sea surface area within two consecutive annular footprint, $A_{ocean}(i,j)$, is actually a polygon and can be estimated the same as the method proposed by Wessel and Smith (1996). The power of each gate, $P(i,j)$, can be roughly compensated by:

$$Comp\_P(i,j) = \frac{P(i,j)}{\rho(i,j)} \ , \tag{3-5}$$

where $\rho(i,j)$ represents the $A_{ocean}(i,j)/A_{ann}$ ratio. The area of each annular footprint, A_{ann}, remain unchanged and can be expressed as:

$$A_{ann} = \frac{\pi c \tau h}{(1+h/R_e)} \ , \tag{3-6}$$

where τ is the width of pulse.

The compensated waveform and the correspounding fitted Brown waveform are shown in Figure 3-6. Compared with Figure 3-4b, not only leading edge, the trailing edge of compensated waveform also shows well agree with the fitted Brown waveform. The difference of three main parameters, range, SWH and σ_0, derived from the masked waveform (Figure 3-4b) and compensated waveform (masked - compensated) are calculated. Results show that the power deficit mainly influence the σ_0 and SWH estimation but slightly for range estimation. However, it is hard to validate the σ_0 estimation due to the lack of in situ measurement. Therefore, only the range estimation is compared and validated in the next section.

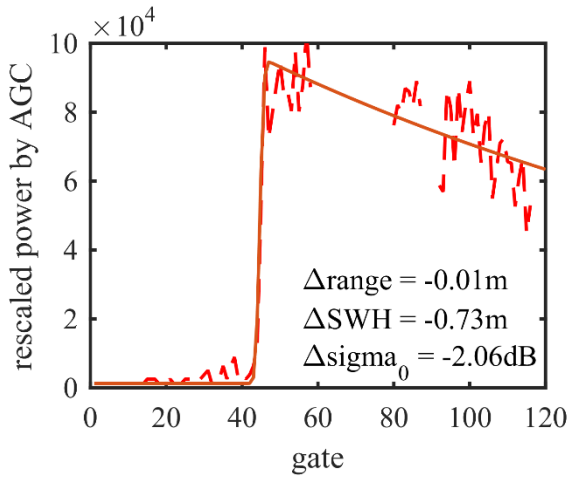

Figure 3-6. The same as Figure 3-4 but for the compensated waveform measured at 34.2ºN as shown in Figure 3-5 (red point as shown in Figure 3-3a).

After removing the calm waveter reflections and compensating waveform power deficit, the along-track SSH can be obtained through range estimation (details see the handbook of Jason-2 product). An unweighted least-square estimator whose convergence is sought through the Nelder-Mead algorithm is adopted in the present study. Figure 3-7 shows the variation of the derived along-track SSH for three different methods over Tsushima islands. Black line represents the result of that provide in SGDR product which derived from the conventional ocean retracker using the full waveform. It is obviously that the ocean retracker failed to estimate the corrupted waveforms near the coast. Blue line represents the result of that provide in ALES product. Only the sub-waveform around waveform leading edge is used for ALES retracker. Red line represents the result of this study. Both the methods of ALES and this study successfully extend the capability of range estimation to the coast. However, a large variation appeared especially for ALES when altimeter closely proximity to the coast, in other word, when echoes around waveform leading edge are corrupted.

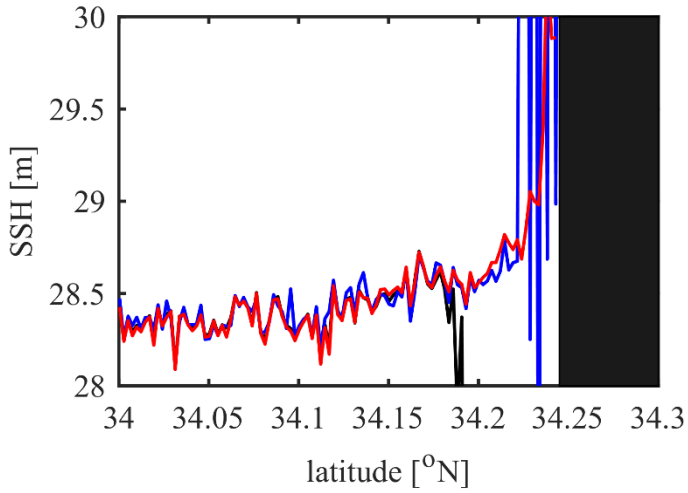

Figure 3-7. Along-track SSH derived from pass 36 cycle 22 of Jason-2 data over Tsushima islands for three different methods. Black is the result of SGDR product, blue is the result of ALES product and red is the result of this study.

3.4 Results and Discussion

In order to validate the quality of range estimation, the sea surface height anomaly (SSHA) along track are calculated as follows:

$$\mathrm{SSHA} = \mathrm{SSH} - \overline{\mathrm{SSH}}, \tag{3-7}$$

where $\overline{\mathrm{SSH}}$ is the mean SSH from cycle 1 to cycle 252. In order to compare with tide gauge measurements, the tidal component unremoved from altimeter measurements.

Two statistics, correlation coefficient (CC) and root mean square difference (RMSD) between the time series of SSHA derived from altimeter and tide gauge measurements, are used to validate the data quality as in Fenoglio et al (2010).

Figure 3-8(a) is the CC variation along track over Tsushima islands for the three different methods. Figure 3-8(b) is the RMSD in centimeters. The same as in Figure 3-7, black lines represent the SGDR results, blue lines represent ALES results and red lines are the results of this study. Results show that the ocean retracker cannot provide the correct estimation within 10km from the coastline (from 34.11ºN to the coast), which approximately corresponding to the radius of altimeter footprint.

As ALES retracker use only the sub-waveform around leading edge, the noise firstly appeared at waveform trailing edge when altimeter proximity to land almost have no influence on range estimation. Results show that ALES extend the range estimation to about 7km from the coastline. However, ALES estimation window is only dependent on the SWH, echoes within the

estimation window are used whether they are corrupted or not. As shown in Figure 9, once the echoes used for estimation are corrupted, it will seriously influence the accuracy of range estimation due to fewer echo number.

In the present study, the range is estimated based on the modified waveforms, results show that CC remains larger than 0.9 (99.9% confidence level) even at locations only about 3km depart from coast. Overall, both the CC and RMSD comparison show that this method is more effective at coastal area very closed to land comparing with ocean retracker and ALES retracker.

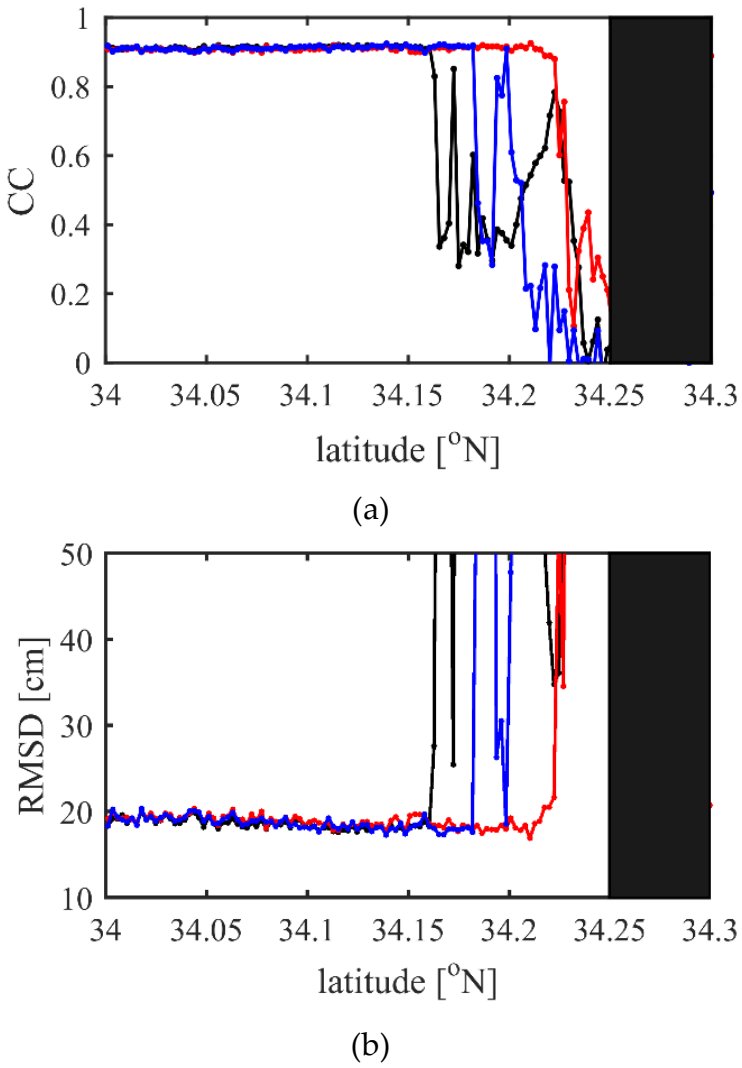

Figure 3-8. Correlation coefficient (CC) (a) and Root mean square difference (RMSD) (b) of sea surface height anomaly (SSHA) derived from tide gauge and altimeter measurements for three different methods. Black is the result of SGDR product, blue is the result of ALES product and red is the result of this study.

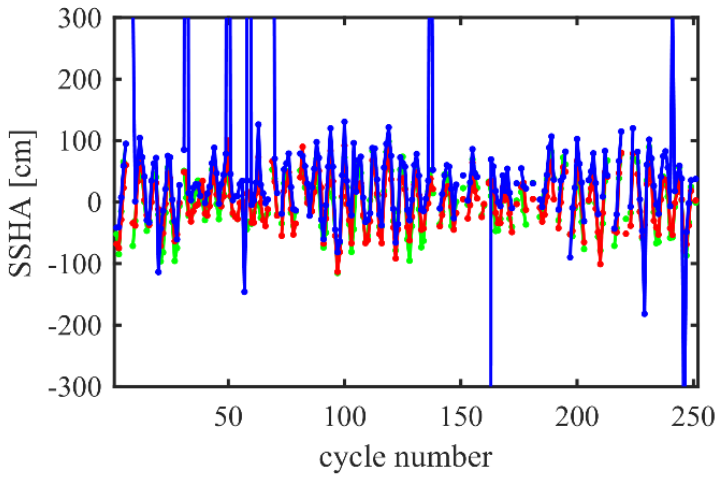

Figure 3-9. Comparison of SSHA time series derived from ALES retracker (blue) and this study (red) at 34.11ºN with tide gauge measurements (green).

3.5 Conclusions

Generally, geophysical parameters can be correctly obtained through waveform retracking using the theoretical Brown model over the open ocean. However, altimeter waveforms are always corrupted at coastal zone due to the heterogeneous surface roughness within altimeter footprint. In particular, reflections from calm waters whose power exceed the leading edge will influence the accuracy of waveform retracking.

Different from the traditionally retrackers which used the individual waveforms, these noises caused by calm waters are explicitly detected and removed utilizing its parabolic signature in the present study. As shown in Figure 3-4b, the leading edge of modified waveform shows well agree with fitted Brown waveform. In other word, the redundant peak echoes are the main factor that influence the range estimation. However, results also show that the modified waveform underestimated the backscatter intensity due to power deficit of waveform trailing edge. In Section 3.3.2, the power deficit of waveform trailing edge due to weak land reflection within altimeter footprint are also compensated. Compared with Figure 3-4b, the trailing edge of compensated waveform also well agree with the fitted Brown waveform (Figure 3-6).

Finally, The SSHA of Jason-2 altimeter over Tsushima in Japan obtained from three different method are compared with the in situ tide gauge measurements. Results showed that our method better agree with tide gauge data than conventional ocean retracker and ALES retracker. The CC remains larger than 0.9 even at about 3km sea area depart from the land. RMSD is about 20cm. Compared with the previous retrackers, this method is useful for the

study of regional oceanography, because it is important to obtain more available data over coastal zone.

4. Conclusions

The waveform data is fundamental to the altimeter geographical parameters retrieval. Over the open, three main parameters, range, SWH and backscatter coefficient σ_0, can be accurately derived from the processing of waveform retracking. Besides of them, recent study has proved that a wave period parameter can be derived from altimeter σ_0 and SWH measurements. However, the altimeter-derived wave period is lower than buoy measurements especially in low-wind conditions.

In fact, altimeter σ_0 is inversely proportional to the wind speed. In particular, it will sharply increase when the small size sea waves is absent from sea surface. In other word, σ_0 of Ku-band radar altimeter is sensitive to the high-frequency sea waves ride on swell in low wind conditions. On the other hand, buoy measurements cannot measure the high-frequency waves due to its relative large size. Therefore, the discrepancy between altimeter and buoy wave period will be significantly depend on local wind filed. Results of this thesis show that, altimeter-derived wave period agree well with buoy measurements when the high-frequency sea waves missed by buoy is compensated. This result is useful for the validation of radar altimeter backscatter measurements by in situ buoy measurements. Moreover, the altimeter-derived wave period may beneficial to the studies on air-sea interaction and wave models etc., where the small size sea waves will play an important role.

Moreover, as the radar altimeter σ_0 is sensitive to high-frequency sea waves, the small space scale variation will occur at locations where sigma0-bloom events or rain cells take place over the open ocean, and in particular, the semi-closed sea along coastal area. The highly reflective sea surface over calmed semi-closed seas is also known as calm water. It is the main reason that caused waveforms deviate from the expected shape over the open ocean. In addition, the weak land reflection will lead the waveform trailing edge fast decrease. Both of them influence the correct retrieval of geophysical parameters over coastal zone.

It is important to obtain as far as more available data over coastal zone for the study of reginal oceanography. Therefore, different from the sub-waveform retracker which were developed for global data processing, we proposed a more sophisticated waveform retracking method for specific sea areas of interest. Results over Tsushima islands in Japan for Jason-2 altimeter data show that, the method of this study is efficient to obtain more available data over coastal zone than MLE4 and ALES method. The CC between SSHA derived by our method is larger than 0.9 even at about 3km depart from coastline of Tsushima.

References

Amarouche, L., Thibaut, P., Zanife, O.Z., Dumont, J.-P., Vincent, P. & Steunou, N. Improving the Jason-1 ground retracking to better account for attitude effects. Marine Geodesy. 2004, 27, 171–197.

Badulin, S. I. A physical model of sea wave period from altimeter data, J. Geophys. Res. Oceans. 2014, 119, 856– 869.

Barrick, D. Wind dependence of quasi-specular microwave sea scatter. IEEE Trans. Antennas Propag. 1974, 22, 135–136.

Bao, L.; Lu, Y.; Wang, Y. 2009. Improved retracking algorithm for oceanic altimeter waveforms. Progress in Natural Science 19 (2):195-203.

Brown, G. The average impulse response of a rough surface and its applications.

IEEE Trans. Antennas. Propag. 1977, 25, 67-74.

Boggs, P.T.; Rogers, J.E. Orthogonal distance regression. Contemp. Math 1990, 112, 183–194.

Caires, S.; Sterl, A.; Gommenginger, C.P. Global ocean mean wave period data: Validation and description. J. Geophys. Res. 2005, 110.

Carter, D.J.T. Development of Procedures for the Analysis of ERS-1 Radar Altimeter Wind and Wave Data, Using GEOSAT Data; Study Rep. 8315/89/HE-I; Europe Space Agency: Paris, France, 1990.

Challenor, P.G.; Srokosz, M.A. Wave studies with radar altimeter. Int. J. Remote Sens. 1991, 12, 1671–1686.

Challenor, P. G., and P. D. Cotton, The joint calibration of altimeter and in situ wave heights, in Advances in the Applications of Marine Climatology—The Dynamic Part of the WMO Guide to the Applications of Marine Climatology, WMO/TD-No. 1081 JCOMM Tech. Rep. No. 13, World Meteorol. Organ., Geneva, 2002.

Chelton, D.B.; Walsh, E.J.; Macarthur J.L. Pulse compression and sea level

tracking in satellite altimetry. J. Atmos. Oceanic Technol. 1989, 6, 407–438.

Clarizia, M. P. Investigating the effect of ocean waves on GNSS-R microwave remote sensing measurement. Ph.D. Thesis, University of Southampton, Southampton, UK, 2012.

Collard, F.; Ardhuin, F.; Chapron, B. Extraction of coastal ocean wave fields from SAR images. IEEE J. Ocean. Eng. 2005, 30, 526–533.

Davies, C. G., Challenor, P. G., Cotton, P. D. Measurements of wave period from radar altimeters. Ocean Wave Measurement and Analysis, B. L. Edge and J. M. Hemsley, Eds. Reston, VA: ASCE, 1997, pp. 819–826.

Deng, X.; Featherstone, W.E. A coastal retracking system for satellite radar altimeter waveforms: application to ERS-2 around Australia. J. Geophys. Res. 2006, 111, C06012.

Fenoglio-Marc, L.; Fehlau, M., Ferri, L., Becker, M., Gao, Y.; Vignudelli, S. Coatal sea surface heights from improved altimeter data in the Mediterranean Sea. Gravity, geoid and earth observation. 2010, 135, 253-261.

Fu, L.L.; Cazenave, A. Satellite altimetry and earth science. ACADEMIC Press. 2001, 11-14.

Gomez-Enri, J.; Vignudelli, S.; Quartly, G.D.; Gommenginger, C.P.; Cipollini, P.; Challenor, P.G.; Benveniste, J. Modeling Envisat RA-2 waveforms in the coastal zone: case study of calm water contamination. IEEE J. Geos. Remote Sens. Letters. 2010, 7, 474-478.

Gommenginger, C.P.; Srokosz, M.A.; Challenor, P.G.; Cotton, P.D. Measuring ocean wave period with satellite altimeters: A simple empirical model. Geophys. Res. Lett. 2003, 30.

Gommenginger, C.; Thibaut, P.; Fenoglio-Marc, L.; Quartly, G.; Deng, X.; Gomez-Enri, J.; Challenor, P.; Gao, Y. Retracking Altimeter Waveforms Near the Coasts. A Review of Retracking Methods and Some Applications to Coastal Waveforms. In Coastal Altimetry. 2011, 61-75.

Govindan, R.; Kumar, R.; Basu, S.; Sarkar, A. Altimeter-Derived Ocean Wave Period Using Genetic Algorithm. IEEE Geoscience and Remote Sensing Letters. 2011, 8(2), 354-358.

Halimi, A.; Mailhes, C.; Tourneret, J.; Thibaut, P.; Boy, F. Parameter estimation for peaky altimetric waveforms. IEEE Trans. Geos. Remote Sens. 2013, 51, 1568-1577.

Hasselmann, 1976. Stochastic climate models Part I. Theory. Tellus. 1976, 28(6), 473–485.

Hayne, G.S. Radar altimeter mean return waveforms from near-normal-incidence ocean surface scattering. IEEE Trans. Antennas. Propag. 1980, 28, 687-692.

Holthuijsen, L.H. Waves in Oceanic and Coastal Waters, 1st ed.; Cambridge University Press: Cambridge, UK, 2007.

Hwang, P.A.; Teague, W. J.; Jacobs, G. A. A statistical comparison of wind speed, wave height and wave period derived from satellite altimeters and ocean buoys in the Gulf of Mexico region. J.Geophys.Res. 1998, 103, no. C5, 10451–10468.

Hwang, P.A.; Wang, D.W.; Walsh, E.J.; Krabill, W.B.; Swift, R.N. Airborne measurements of the wavenumber spectra of ocean surface waves. PartI: Spectral slope and dimensionless spectral coefficient. J. Phys. Oceanogr. 2000, 30, 2753–2767.

Hwang, P. A.; Wang, D. W. Directional distributions and mean square slopes in the equilibrium and saturation ranges of the wave spectrum. J. Phys. Oceanogr. 2001, 31, 1346–1360.

Hwang, C.; Guo, J.Y.; Deng, X.L.; Hsu, H.Y.; Liu, Y.T. Coastal gravity anomalies from retracked Geosat/GM altimetry: improvements, limitation and the role of airborne gravity data. J. Geod. 2006, 80, 204-216.

Idris, N.; Deng, X.L. The retracking technique on multi-peak and quasi-specular waveforms for Jason-1 and Jason-2 missions near the coast. Mar. Geod. 2012, 35, 217-237.

Klein, L.A.; Swift, C.T. An improved model for the dielectric constant of sea water at microwave frequencies. IEEE J. Ocean. Eng. 1977, 25, 104–111.

Krogstad, H.E., Barstow, S.F. Satellite wave measurements for coastal engineering applications. Coastal Engineering. 1999, 37, no. 3-4, pp. 283-307.

Kshatriya, J.; Sarkar, A.; Kumar, R. Determination of Ocean Wave Period from Altimeter Data Using Wave-Age Concept. Marine Geodesy. 2005, 28:1, 71-79.

Li, S.Q.; Zhao, D.L.; Zhou, L.M.; Liu, B. Dependence of mean square slope on wave state and its application in altimeter wind speed retrieval. Int. J. Remote Sens. 2013, 34, 264–275.

Lee, H.; Shum, C. K.; Yi, Y.; Braun, A.; Kuo, C.Y. 2008. Laurentia crustal motion observed using Topex/Poseidon radar altimetry over land. Journal of Geodynamics 46 (3-5):182-193.

Mackay, E.B.L.; Retzler, C.H.; Challenor, P.G.; Gommenginger, C.P. A parametric model for ocean wave period from Ku band altimeter data. J. Geophys. Res. 2008, 113.

Martin, T.V., H.J. Zwally, A.C. Brenner, and R.A. Bindschadler. 1983. Analysis and retracking of continental ice sheet radar altimeter waveforms. Journal Geophysical Research 88 (C3):1608-1616.

Mitchum, G., D. Hancock, G. Hayne, and D. Vandemark (2004), Blooms of sigma0 in the TOPEX radar altimeter data, J. Atmos. Oceanic Technol., 21, 1232–1245.

Nondirectional and Directional Wave Data Analysis Procedures, National Buoy Data Center (NDBC) Technical Document 96-01; Neptune Sciences Inc.: Slidell, LA, USA, 1996; p. 37.

OSTM/Jason-2 Products Handbook; Le site du Centre national d'études spatiales (CNES): Paris, France, 2015.

Passaro, M.; Cipollini, P.; Vignudeli, S.; Quartly, G.D.; Snaith, H.M. ALES: A multi-mission adaptive subwaveform retracter for coastal and open ocean altimetry. Remote Sens. Environ. 2014, 145, 173-189.

Phillips, O.M. The Dynamics of the Upper Ocean, 2nd ed.; Cambridge University Press: Cambridge, UK, 1977.

Phillips, D.M. Effects of the wavenumber spectrum of a sea surface on Laser Beam Reflection. Aust. J. Phys. 1979, 32, 469–489.

Phillips, O.M. Spectral and statistical properties of the equilibrium range in wind-generated gravity waves. J. Fluid. Mech. 1985, 156, 505–531.

Quartly, G.D. 2008. Optimizing σ0 information from the Jason-2 altimeter. IEEE Geoscience & Remote Sensing Letters. 2008.

Quartly, G.D. 2010. Hyperbolic retracker: removing bright target artifacts from altimetric waveform data. In Proceeding of ESA Living Planet Symposium, June in Bergen. ESA SP-686.

Quilfen, Y.; Chapron, B.; Serre, M. Calibration/validation of an altimeter wave period model and application to TOPEX/Poseidon and Jason-1 altimeters. Mar. Geod. 2004, 27, 535–549.

Raney, R.K. Radar Altimeter Fundamentals and Near-Shore Measurements. Poster on 1st Coastal Altimetry Workshop. 2008.

Roca, M; Francis, R; Zelli, C; Laxon, S; Jackson, H. RA-2 absolute range and sigma-0 calibration and in-flight verification. European Space Agency, (Special Publication) (461). 2000, 2310-2326.

Sarkar, A.; Kumar, R.; Mohan, M. Estimation of wave periods by space-borne altimeters. Indian J. Mar. Sci. 1998, 27, 43–45.

Toba, Y. Local balance in the air-sea boundary process, I. On the growth process of wind waves. J. Oceanogr. Soc. Japan. 1972, 28, 109–120.

Tournadre, J. Determination of rain cell characteristics from the analysis of TOPEX altimeter echo waveforms. J. Atmos. Oceanic Technol. 1998, 15, 387-406.

Tournadre, J., B. Chapron, N. Reul, and D. C. Vandemark (2006), A satellite altimeter model for ocean slick detection, J. Geophys. Res., 111, C04004.

Tournadre, J. Signature of lighthouses, ships, and small islands in altimeter

waveforms. J. Atmos. Oceanic Technol. 2007, 24, 1143-1149.

Tourneret, J. Y., C. Mailhes, J. Severini, and P. Thibaut. 2010. Shape classification of altimetric signals using anomaly detection and Bayes decision rule. In Proceedings of Geosciences and Remote Sensing Symposium (IGARSS), July in Hawaii, USA, IEEE International.

Tran, N., D. W. I. Hancock, G. S. Hayne, D. W. Lockwood, D. Vandemark, M. L. Driscoll, and R. V. Sailor (2002), Assessment of the cycle-to-cycle noise level of the Geosat Follow-On, TOPEX, and Poseidon altimeters, J. Atmos. Oceanic Technol., 19, 2095–2107.

Tseng, K.H.; Shum, C.K.; Yi, Y.C.; Emery, W.J.; Kuo, C.Y.; Lee, H.; Wang, H.H. The improved retrieval of coastal sea surface heights by retracking modified radar altimetry waveforms. IEEE Trans. Geos. Remote Sens. 2014, 52, 991-1001.

Tucker, M.J. Waves in Ocean Engineering: Measurement, Analysis, Interpretation, 1st ed.; Ellis Horwood Ltd.: Chichester, UK, 1992.

Vendemark, D.; Chapron, B.; Sun, J.; Crescenti, G.H.; Graber, H.C. Ocean wave slope observations using radar backscatter and laser altimeters. J. Phys Oceanogr. 2004, 34, 2825–2842.

Cipollini, P. et al. Progress in Coastal Altimetry: the experience of the COASTALT Project. Geophysical Research Abstracts. 2009, 11, EGU2009-12862. EGU General Assembly.

Vignudelli, S.; Cipollini, P.; Astrald,i M.; Gasparini, G.P.; Manzella, G.M.R. Integrated use of altimeter and in situ data for understanding the water exchanges between the Tyrrhenian and Ligurian Seas. J Geophys Res. 2000, 105:19,649–19,000.

Vignudelli S., Kostianoy A.G., Cipollini P., Benveniste, J. Coastal Altimetry. 2011, Springer Heidelberg Dordrecht London New York.

Wessel, P.; Smith, W. H. F. A Global Self-consistent, Hierarchical, High-resolution Shoreline Database, J. Geophys. Res. 1996, 101, 8741-8743.

Wu, J. Wind-stress coefficients at light winds. J. Atmos. Ocean. Technol. 2009, 5, 885–888.

Yang, L.; Lin, M.S.; Liu, Q.H.; Pan, D.L. A coastal altimetry retracking strategy based on waveform classification and sub-waveform extraction. Inter. J. Remote Sens. 2012, 33, 7806-7819.

Zhao, D. (2002): Preliminary study on wave characteristics in natural conditions. J. Ocean Univ. Qingdao, 32(6), 853– 858 (in Chinese with English abstract).